# ENTANGLEMENT-LOOSENING DYNAMICS RESOLVED THROUGH COMPARISON OF DIELECTRIC AND VISCOELASTIC DATA OF TYPE-A POLYMERS: A REVIEW

YUMI MATSUMIYA, HIROSHI WATANABE\*
INSTITUTE FOR CHEMICAL RESEARCH, KYOTO UNIVERSITY, UJI, KYOTO 611-0011, JAPAN

RUBBER CHEMISTRY AND TECHNOLOGY, Vol. 93, No. 1, pp. 22-62 (2020)

#### **ABSTRACT**

For so-called type-A polymer chains having electrical dipoles aligned parallel along their backbone, the large-scale chain motion over the end-to-end distance results in not only viscoelastic but also dielectric relaxation. These two relaxation processes detect the same motion but with different averaging moments, which enables us to *experimentally* resolve some details of the chain dynamics through comparison of viscoelastic and dielectric data of type-A polymers. For a typical type-A polymer, high-*cis* polyisoprene (PI), results of such an experimental approach are summarized to discuss characteristic features of an entanglement-loosening process (constraint release and/or dynamic tube dilation process) resolved from the data comparison. [doi:10.5254/rct.19.80388]

#### CONTENTS

I.	Introduction	22
II.	Results and Discussion	25
	A. Relaxation Mechanisms in Tube Model	25
	B. Test of Fixed Tube Model	26
	C. Experimental Observation of Constraint Release Relaxation	27
	1. Overview	27
	2. Data of CR Relaxation Time	32
	3. Factors Determining CR Relaxation Time	34
	D. Experimental Test of Dynamic Tube Dilation Mechanism	39
	1. Test of Molecular Picture of Full-DTD	41
	2. Test of Molecular Picture of Partial-DTD	44
	E. Duality of Tube for Relaxation Time and Relaxation Intensity	49
	1. Viscoelastic and Dielectric Data of Linear PI Probe in DTD-Free Environment	50
	2. Relaxation Time in DTD-Free Environment	53
	3. CR–Rouse Analysis of Relaxation Time	55
	F. Comments on Recent Theoretical Model/Analysis	57
	1. Tube Dilation Exponent and Feature of Interchain Constraint	57
	2. Duality in Description of Reptation along Tube	59
III.	Concluding Remarks	60
IV.	Acknowledgements	60
	References	60

# I. INTRODUCTION

Needless to say, flexible polymer chains exhibit active thermal motion at temperatures well above their glass transition temperature ( $T_{\rm g}$ ). This thermal motion, occurring in various length scales spanning from the monomeric bond length to the end-to-end distance of the whole chain backbone, is the origin of macroscopically observed relaxation processes, for example, viscoelastic and dielectric processes.<sup>1,2</sup> These processes average the same thermal motion of

<sup>\*</sup>Corresponding author. Email: hiroshi@scl.kyoto-u.ac.jp

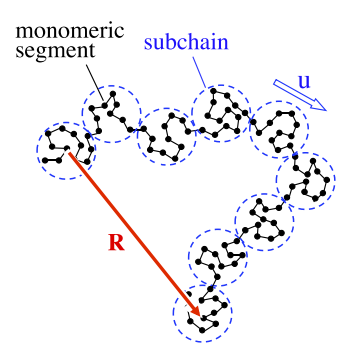


FIG. 1. — Schematic illustration of the chain and subchain.

the chains but in different ways, which enables us to experimentally resolve some details of the chain dynamics through comparison of those processes. For example, in short time scales, comparison of viscoelastic and dielectric data may allow us to resolve the chemical group(s) involved in the local relaxation. The dielectric relaxation is activated mostly by motion of polar groups, whereas the viscoelastic relaxation is essentially irrelevant to the polarity, so that comparison of the dielectric and viscoelastic relaxation intensities provides us with a clue for specifying the chemical group(s) responsible for the observed relaxation. For example, the beta relaxation of poly(methyl methacrylate) (PMMA) is detected in both viscoelastic and dielectric data, but the relaxation intensity is much larger (compared to the alpha relaxation) in the dielectric data, which suggests that the rotational motion of the COOCH<sub>3</sub> group (coupled with local torsion of the backbone) is the origin of the beta relaxation of PMMA.<sup>3</sup>

The above example shows that the local relaxation in the length scale of monomeric bonds sensitively reflects the chemical structure of the polymer chain. In contrast, the global (large-scale) relaxation over the end-to-end distance of the chain backbone is rather insensitive to the chemical structure<sup>1,4</sup> (except for  $T_g$  that determines the friction factor for the global relaxation). Consequently, the global relaxation is *universal* for a wide variety of chemically different polymers and has been considered to be described by only a few parameters. <sup>1,4</sup> For example, the linear viscoelastic terminal relaxation of entangled, monodisperse linear polymers is described by the entanglement plateau modulus  $G_N$  and the terminal relaxation time  $\tau$  ( $\sim \tau_e N^{3.5}$ ), with  $\tau_e$  and N being the Rouse relaxation time of an entanglement segment and the number of those segments per chain, respectively.<sup>4,5</sup>

For molecular description of the entanglement relaxation, this universality allows us to divide the chain backbone into "subchains," as schematically illustrated in Figure 1. In general, we can use subchains of *any* size in description of the flexible chain dynamics, given that each subchain contains a sufficiently large number of Kuhn segments (to behave as a flexible unit) and is internally equilibrated (through motion of those segments) in a focused time scale. Because of this freedom in the choice of subchain, the entanglement segment, having a known molecular weight  $M_e$  and sustaining the plateau modulus, is conveniently used in literature (and in this article) as the subchain when our focus is placed on the chain dynamics in a length scale larger than the entanglement length. Then, the chain backbone is expressed as a sequence of N subchains ( $N = M/M_e$  with M being the chain molecular weight), and the dynamics is described as the time evolution of the subchain bond vectors  $\mathbf{u}(n,t)$ , with n being the subchain index (0 < n < N). Specifically, in the linear viscoelastic regime, those subchains behave as Gaussian chains, and their relaxation modulus G(t), measured after imposition of a small step

shear strain  $\gamma$  at time 0, is expressed in terms of the shear component of the dyadic of **u**. In a continuous treatment, this expression reads<sup>1,2</sup>

$$G(t) = \frac{1}{\gamma} \left( \frac{3vk_{\rm B}T}{a^2} \right) \int_0^N \langle u_x(n,t)u_y(n,t) \rangle_{\gamma} \mathrm{d}n \tag{1}$$

where  $a^2 = \langle \mathbf{u}^2 \rangle_{\rm eq}$  (average at equilibrium),  $\nu$  is the chain number density,  $k_{\rm B}$  and T indicate the Boltzmann constant and absolute temperature, and  $\langle \cdots \rangle_{\gamma}$  stands for the average taken for all chains under the strain. Equation 1 is equivalent to the stress-optical rule<sup>6</sup> at sufficiently long times where each subchain is internally equilibrated.

A brief comment may need to be made for a molecular meaning of Eq. 1.  $^{1,2}$  At equilibrium, the subchains in a polymeric material are isotropically oriented (and in the Gaussian state) so that their entropic tensions are balanced in all directions. Thus, the material exhibits no macroscopic stress  $\sigma(t)$  in an undeformed, equilibrium state at t < 0. The step strain distorts this orientational distribution of the subchains to disrupt the tension balance, and an unbalanced part of the tension reflecting the anisotropy of the subchain orientation is observed as the macroscopic  $\sigma(t)$ . For the shear strain considered here, the factor  $\langle u_x(n,t)u_y(n,t)\rangle$  (shear component of the dyadic  $\langle \mathbf{u}\mathbf{u}\rangle$ ) specifies the isochronal orientational anisotropy of n-th subchain at time t, and  $\sigma(t) (= \gamma G(t))$  is expressed as a sum of this factor for all subchains, as shown in Eq. 1. Correspondingly, the relaxation of G(t) reflects decay of the orientational anisotropy of the subchains occurring through their thermal motion.

The same motion of the subchains also activates dielectric relaxation, given that the subchains have so-called type-A dipoles parallel along the chain backbone. Specifically, for type-A linear chains without dipole inversion, a microscopic polarization of the chain is proportional to its end-to-end vector  $\mathbf{R}(t) = \int_0^{N} \mathbf{u}(n,t) dn$  (cf. Figure 1). Thus, the dielectric relaxation function F(t), measured after imposing a weak electric field E for  $-\infty < t < 0$  in y direction and removing the field at t = 0, is expressed in terms of the y component of the subchain bond vector  $\mathbf{u}(n,t)$  as

$$F(t) = \frac{v}{E} \int_0^N m_{\rm d} \langle u_{\rm y}(n,t) \rangle_E {\rm d}n \tag{2}$$

In Eq. 2,  $m_{\rm d}$  is the magnitude of dipole per unit length of the chain backbone, and a factor  $m_{\rm d}u_y(n,t)$  denotes the polarization of the n-th subchain at time t.  $\langle {}^{...} \rangle_E$  stands for the average taken for all chains during the relaxation process after removal of the electric field, and the integral in Eq. 2 gives the average polarization of the type-A chain.

Comparing Eqs. 1 and 2, we note that the viscoelastic and dielectric relaxation processes of type-A chains detect the same motion of the chain (the dynamics of  $\mathbf{u}$ ) but with different averaging moments, the second- and first-moment averages of  $\mathbf{u}$  at time t. This difference enables us to experimentally resolve some details of the global dynamics of the type-A chain through comparison of the viscoelastic and dielectric data. For convenience of this comparison, this article uses an expression of the normalized dielectric relaxation function  $\Phi(t)$  deduced from the fluctuation–dissipation theorem,  $^{1,2,8}$ 

$$\Phi(t) \equiv \frac{F(t)}{F(0)} = \frac{1}{Na^2} \int_0^N \int_0^N \langle \mathbf{u}(n,t) \cdot \mathbf{u}(n',0) \rangle_{\text{eq}} dn dn'$$
(3)

where F(0) is the initial value of F(t), and  $\langle \cdots \rangle_{eq}$  stands for the average taken at equilibrium where all chains have an isotropic Gaussian conformation dynamically fluctuating with time. (This  $\Phi(t)$  represents the first-moment average of  $\mathbf{u}(n,t)$  at time t, as is the case also for F(t).) Equations 2 and 3 are rigorously equivalent to each other, but the Gaussian feature underlying Eq. 3 is more convenient, compared to the oriented conformation (created by the electric field) considered in Eq.

2, for analyzing the chain dynamics. Thus, in this article, the comparison of viscoelastic and dielectric data of entangled type-A polymer is mainly made for  $\Phi(t)$  described by Eq. 3 and the normalized viscoelastic relaxation function,  $\mu(t) \equiv G(t)/G_N$  with G(t) given by Eq. 1. (The fluctuation–dissipation theorem gives an expression of  $\mu(t)$  in terms of  $\mathbf{u}$  at equilibrium [that corresponds to Eq. 3], but this expression is not used in this article.)

We find a considerable variety of type-A chains that include poly(propylene oxide), poly(phenylene oxide), poly( $\varepsilon$ -caprolactone), and high-cis polyisoprene. <sup>10</sup> Nevertheless, for the first three polymers, we note some difficulties in the dielectric measurements in a melt state: in general, the measurements at high temperatures (T) are disturbed by a direct current conduction due to ionic impurities so that the type-A polymer to examine is desired to behave as an amorphous melt at low T. Namely, the polymer is desired to have a low  $T_g$  (and a low melting temperature if it is semi-crystalline). The first three in the above list are not very convenient from this experimental viewpoint. In contrast, synthetic polyisoprene (PI), obtained from living anionic polymerization in non-polar solvents, is rich in the cis microstructure (cis-1,4:trans-1,4:vinyl-3,4  $\cong$  80:15:5)<sup>11</sup> to have the type-A dipole of detectable magnitude, and stays as an amorphous melt even at low T because it does not crystallize and has low  $T_g \cong -70^{\circ}\text{C}$ ). Furthermore, for the synthetic PI, samples of various topological architectures (such as a star-branched architecture) with a narrow molecular weight distribution can be prepared rather easily through coupling of living PI anions. In addition, PI chains have only weak (though detectable) type-A dipoles, so that their dynamics is negligibly affected by the dipole-dipole interaction and coincides with that in a typical, non-polar amorphous melt. (PI also has the type-B dipole perpendicular to the chain backbone, <sup>10</sup> but this dipole is also weak, thus not disturbing the amorphous melt dynamics.)

Because of these advantageous features of PI, the slow dielectric relaxation reflecting the global chain dynamics has been extensively examined mostly for PI, <sup>1,10–40</sup> and comparison of the viscoelastic and dielectric data has revealed some details of the dynamics. This review article adopts an experimental viewpoint as much as possible to focus on the details of the entanglement-loosening mechanism resolved from the data comparison <sup>30–40</sup> mainly for entangled linear and star PI. (This experimental approach is unique to the authors' group, and no similar approach is found in literature.) In relation to this mechanism, comparison between chemically different polymers (PI and polystyrene), not fully discussed in literature, is also presented.

Throughout this article, the sample code number indicates the molecular weight. For example, PI 626k and PI 1.1M stand for linear PI samples with  $M=626\times10^3$  and  $1.1\times10^6$ , respectively, and PI  $(80k)_6$  is a six-arm branched star PI sample with the arm molecular weight of  $M_{\rm arm}=80\times10^3$ .

# II. RESULTS AND DISCUSSION

# A. RELAXATION MECHANISMS IN TUBE MODEL

For a given chain (probe) in an entangled system, surrounding chains behave as uncrossable objects. In the tube model widely used as a basic framework for describing the dynamics of such a probe, a topological constraint for the probe motion due to those objects is expressed as an impermeable tube surrounding the probe, and the probe is considered to move in the tube having a diameter identical to the entanglement length a. (The a corresponds to the entanglement plateau modulus;  $G_N \propto c/a^2$ , with c being the mass concentration of the chains.) In this molecular picture, the relaxation is equivalent to thermal escape of the probe from the tube at time 0: namely, the orientational anisotropy and memory shown in Eqs. 1 and 3 vanish on this escape.

In the classical tube model not considering motion of the tube-forming chains, this escape occurs through *reptation* (one-dimensional curvilinear diffusion along the tube) for the linear probe and through *arm retraction* (contraction along the tube) for a star probe; 1,2,4 see Figure 2. The

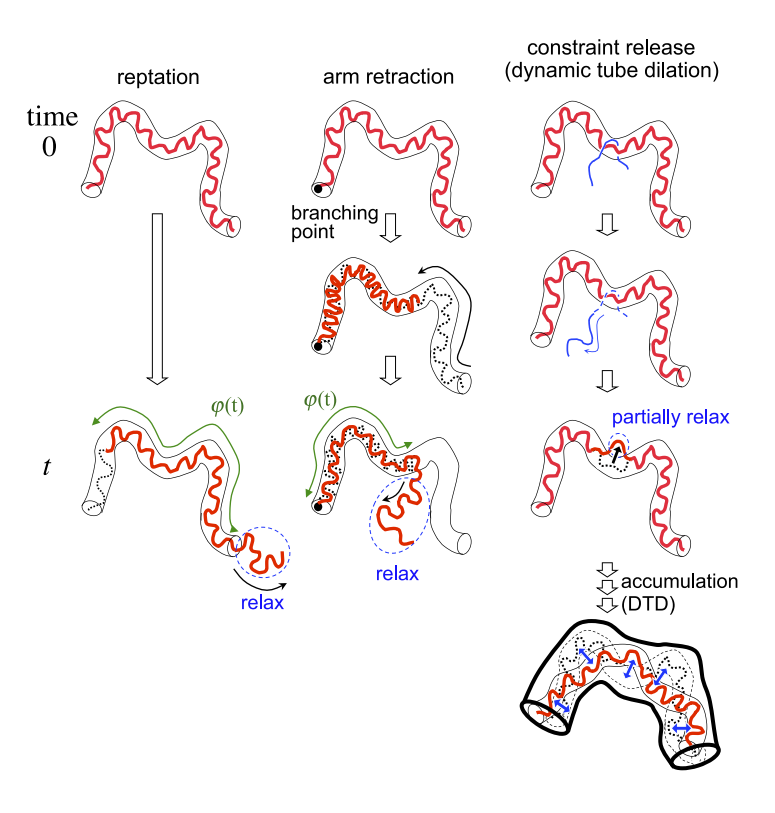


FIG. 2. — Schematic illustration of representative relaxation mechanisms considered in the tube model.

contour length of the linear probe measured along the tube fluctuates with time, and this mechanism (not illustrated in Figure 2) reduces the effective diffusion length of the probe to accelerate the relaxation. A refined tube model considers motion of the tube-forming chains to introduce the *constraint release* (CR) mechanism that allows local hopping of the probe beyond the tube wall; See Figure 2. This CR mechanism introduces a multi-chain nature of the entanglement relaxation into the tube model. Accumulation of such local CR processes effectively widens the tube diameter. This mechanism is referred to as *dynamic tube dilation* (DTD).

# B. TEST OF FIXED TUBE MODEL

For the reptation, contour length fluctuation (CLF), and arm retraction mechanisms occurring in the absence of CR/DTD, we can formulate the time evolution of the bond vector  $\mathbf{u}$  of the entanglement segment (subchain) appearing in Eqs. 1 and 3 to calculate the normalized viscoelastic and dielectric relaxation functions,  $\mu(t) (= G(t)/G_{\rm N})$  and  $\Phi(t)$ . Comparing the calculated  $\mu(t)$  and  $\Phi(t)$  with data, we can test validity of the fixed tube models for real entangled polymers. However, this type of test requires us to consider all possible modes of chain motion simultaneously occurring in the fixed tube; for example, reptation and CLF may not *additively* contribute to  $\mu(t)$ , (i.e., not in a way considered in some models). In addition, we may have some freedom to adjust model parameters in the test. Thus, direct comparison between the model calculation and data is not so easily conducted.

In contrast, comparison of viscoelastic and dielectric data allows us to unequivocally test the fixed tube model. In this model, a subchain at time *t* staying in the surviving portion of the initial

tube preserves the orientational anisotropy and memory of the other subchain that was located at the same position in the initial state (time 0), as can be easily noted in Figure 2. Then, the normalized relaxation functions are identical to the survival fraction of the initial tube  $\varphi(t)$  irrespective of the details of the conformational changes between the times 0 and t,

$$\mu(t) = \Phi(t) = \varphi(t)$$
 for fixed tube model (4)

Equation 4 gives a simple relationship between the normalized storage modulus  $G'(\omega)/G_N$  and the normalized decrease of the dynamic dielectric permittivity  $\{\varepsilon_0 - \varepsilon'(\omega)\}/\Delta\varepsilon$  (with  $\varepsilon_0 = \varepsilon'(0)$  and  $\Delta\varepsilon =$  dielectric intensity), and between the normalized loss modulus  $G''(\omega)/G_N$  and the normalized dielectric loss  $\varepsilon''(\omega)/\Delta\varepsilon$ , all being measured as functions of the angular frequency  $\omega$ , as: 1,24,37,40

$$G'(\omega)/G_{\rm N} = \{\varepsilon_0 - \varepsilon'(\omega)\}/\Delta\varepsilon$$
 (5a)

$$G''(\omega)/G_{\rm N} = \varepsilon''(\omega)/\Delta\varepsilon$$
 (5b)

In Figure 3, these relationships are examined for the viscoelastic and dielectric data of linear PI 308k  $(M=308\times10^3)^{34}$  and six-arm star PI  $(59k)_6$   $(M_{arm}=59\times10^3)^{33}$  both having narrow molecular weight distribution (MWD),  $M_{\rm w}/M_{\rm n}<1.1$ . For simplicity, such narrow MWD samples are hereafter referred to as monodisperse samples.

As noted in Figure 3, the monodisperse linear and star PI samples do not obey Eq. 5; the dielectric relaxation (red symbols) is significantly narrower and slower than the viscoelastic relaxation (blue symbols). Consequently, the entanglement represented as the tube is not fixed in space, and the CR/DTD mechanism explained for Figure 2 plays an essential role in the slow dynamics of those samples. This experimental finding serves as a starting point for a further test of the dynamics of the entangled linear and star polymers. (It should be added that the fixed entanglement environment, wherein Eq. 5 is valid, is realized for dilute probes in high-*M* matrices, as shown later in Figure 23.)

#### C. EXPERIMENTAL OBSERVATION OF CONSTRAINT RELEASE RELAXATION

1. Overview. — The constraint release (CR) relaxation can be most clearly observed for dilute high-M probe chains entangled *only* with much shorter matrix chains. As an example, Figure 4 shows G' and G'' data (symbols) of blends of linear dilute PI 626k probe ( $M_2 = 626 \times 10^3$ ; volume fraction  $v_2 = 0.005$ ) in entangling linear PI matrices with various molecular weights  $M_1$  as indicated. <sup>44</sup> For comparison, the imaginary part of the complex viscosity,  $\eta'' = G'/\omega$ , with  $\omega$  being the angular frequency, is also shown (top panel). The time–temperature superposition excellently worked for those data <sup>44</sup> (and for all other data presented in this review). For the blends, the indices "1" and "2" are hereafter used to represent the short and long chain components, respectively.

As noted in Figure 4, the data of the blends (symbols) with such small  $v_2$  are almost indistinguishable from the matrix data (dashed curves) at high  $\omega$  where the matrix has not relaxed. In contrast, at low  $\omega$  where the matrix has fully relaxed, the relaxation of the dilute PI 626k probe is clearly observed, in particular for G' and  $\eta''$  being much more sensitive to weak but slow relaxation compared to G''. (Thus, G' clearly exhibits a double-step decrease at high and low  $\omega$ , and  $\eta''$  shows two peaks at those  $\omega$ .) We also note that the mode distribution of the probe relaxation is insensitive to  $M_1$  of the matrix given that  $M_1$  is much smaller than  $M_2$  of the probe. In this extreme situation, the probe relaxation is activated by the motion of much shorter matrix chains, namely, pure CR relaxation of the probe is detected experimentally. The corresponding CR behavior of dilute probes has been observed also for the dielectric relaxation of PI probes<sup>26,34</sup> and for the viscoelastic relaxation  $^{45-48}$  and diffusion of polystyrene (PS) probes. Viscoelastic data of binary blends

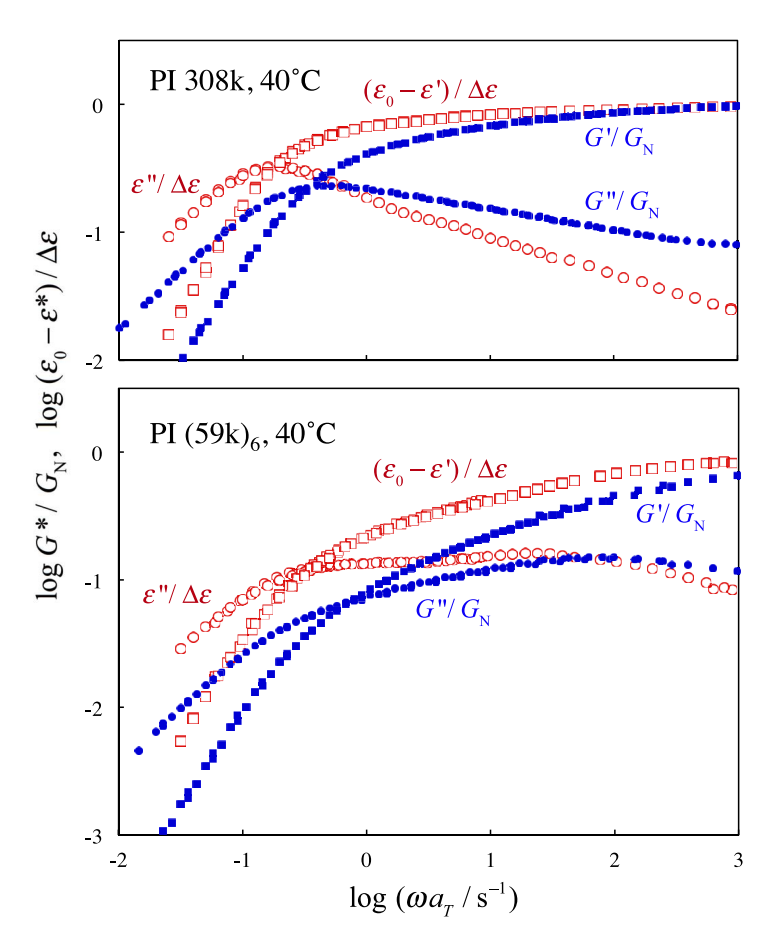


FIG. 3. — Normalized viscoelastic and dielectric data of monodisperse linear PI 308k (top panel) and six-arm star PI  $(59k)_6$  (bottom panel) at 40 °C. The parameters used in normalization are  $\epsilon_0$ =2.41,  $\Delta\epsilon$ =0.10, and  $G_N$ =0.48 MPa. Data are taken from Watanabe et al.  $^{33,34}$  with permission.

have been reported extensively also for the other polymer species, for example, polybutadiene (PB). However, to the best of our knowledge, no systematic data are available for long and *dilute* PB probes entangled *only* with *much shorter* matrix PB chains (i.e., for the dilute PB probes in the CR regime).

For  $v_2$  (=1  $-v_1$ )  $\ll$  1, the behavior of the matrix chains in the blend is negligibly affected by the dilute probe, as noted in Figure 4. Then, the matrix contribution to the complex modulus  $G_b$ \* ( $\omega$ ) of the blend is safely evaluated as  $v_1G_{1,m}$ \* ( $\omega$ ), with  $G_{1,m}$ \* ( $\omega$ ) being the complex modulus data of pure matrix. Correspondingly, the complex modulus of the dilute probe in the blend is obtained from the  $G_b$ \* ( $\omega$ ) and  $G_{1,m}$ \* ( $\omega$ ) data as  $^{34,44-46,51}$ 

$$G_{2,b}^{*}(\omega) = G_{b}^{*}(\omega) - v_{1}G_{1,m}^{*}(\omega)$$
 (6)

Figure 5 compares the storage modulus  $G_{2,b}'(\omega)$  thus evaluated for *dilute* linear PI probes <sup>44</sup> in the CR regime (namely, for the PI probes entangled only with much shorter PI matrix chains). Also shown for comparison is the  $G_{2,b}'(\omega)$  data of PS probes in the CR regime reported in the literature. <sup>45,46</sup> For clarity of the figure, the data are shown only for representative probes. Those PI

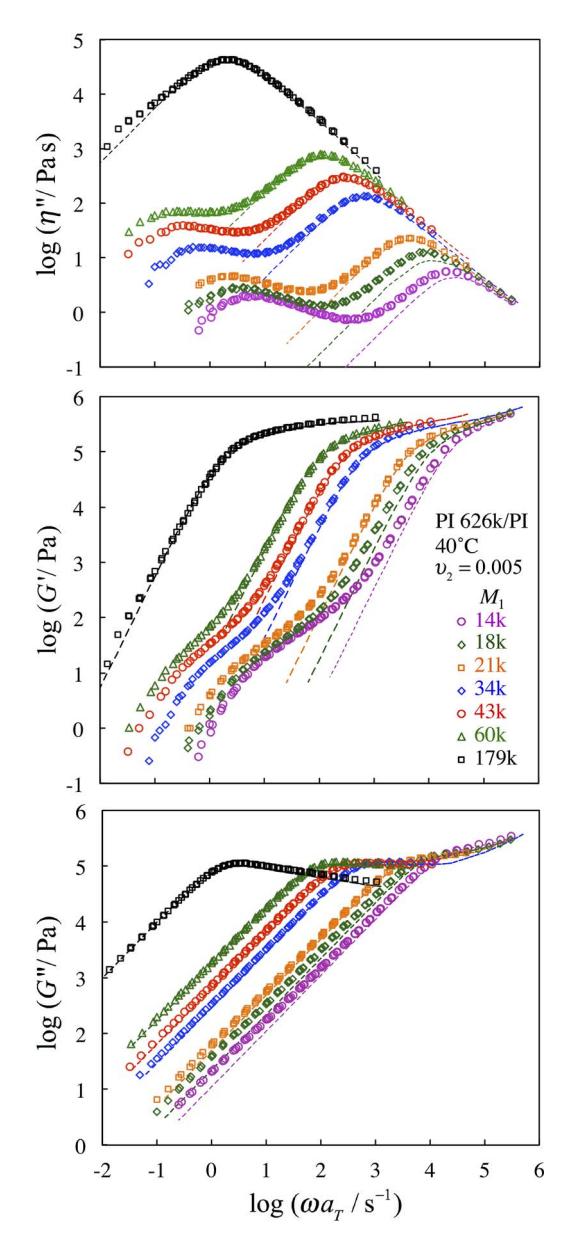


FIG. 4. — Linear viscoelastic data of PI 626k/PI blends at 40 °C (symbols). The volume fraction of the dilute high-M probe (PI 626k) is  $v_2$  = 0.005 in all blends. Dashed curves indicate the data of pure matrix PI. Data are taken from Sawada et al. 44 with permission.

and PS probes have various  $M_2$  and  $\upsilon_2$ , and their  $G_{2,b}'(\omega)$  data were obtained at different temperatures (40 and 167 °C for the PI and PS probes, respectively). Thus, in the comparison in Figure 5, the  $G_{2,b}'(\omega)$  data are normalized by the Rouse factor,  $\{M_2/\rho\upsilon_2RT\}$  with  $\rho$ , R, and T being the mass density of the blend, gas constant, and absolute temperature, respectively, and plotted against the reduced frequency  $\omega\langle\tau_{2,b}^{[G]}\rangle$ . Here,  $\langle\tau_{2,b}^{[G]}\rangle$  is the second-moment average viscoelastic relaxation time of the probe evaluated from the  $G_{2,b}'(\omega)$  and  $G_{2,b}''(\omega)$  data as  $^{34,44-46}$ 

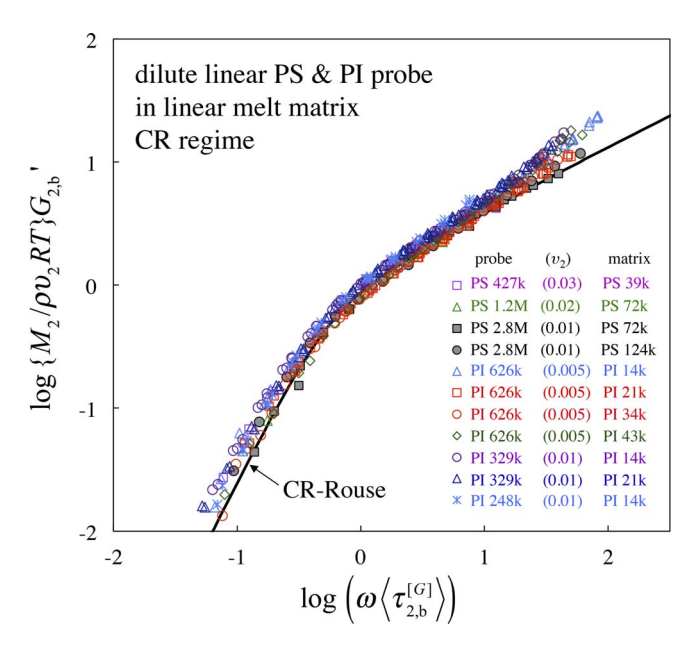


FIG. 5. — Storage modulus  $G_{2^{\circ}b'}$  of dilute linear probe entangled only with much shorter linear matrix chains. The  $G_{2^{\circ}b'}$  data for PI and PS probes (at 40 and 167 °C, respectively) are normalized by the Rouse factor  $\{M_2/\rho v_2RT\}$  and plotted against the reduced frequency,  $\omega \langle \tau_{2,b}^{[G]} \rangle$ . Data are taken from Watanabe et al. <sup>44–46</sup> with permission.

$$\langle \tau_{2,b}^{[G]} \rangle = \left[ \frac{G'_{2,b}(\omega)}{\omega G''_{2,b}(\omega)} \right]_{\omega \to 0}$$

$$= \left\{ \int_0^\infty t G_{2,b}(t) dt \right\} / \left\{ \int_0^\infty G_{2,b}(t) dt \right\}$$
(7)

 $\langle \tau_{2,b}^{[G]} \rangle$  is identical to a ratio of weighed integrals of the relaxation modulus  $G_{2,b}(t)$  of the probe<sup>1</sup> (as shown in the second line of Eq. 7). Note that the subtraction in Eq. 6 is just a minor correction for the  $G_b'(\omega)$  data of the blend at low  $\omega$  examined in Figure 5 (because  $G_b'(\omega) \gg G_{1,m}'(\omega)$  at those  $\omega$ ; see middle panel of Figure 4) and that the normalized modulus  $\{M_2/\rho \upsilon_2 RT\}G_{2,b}'(\omega)$  and the relaxation time  $\langle \tau_{2,b}^{[G]} \rangle$  were experimentally confirmed to be *independent* of  $\upsilon_2$  (see, for example, Watanabe et al.<sup>38</sup> and its Supporting Information, Sawada et al.<sup>44</sup> and Watanabe and Kotaka<sup>45</sup>): namely, the probe was confirmed to be dilute and entangled only with the matrix chains.

In Figure 5, the  $G_{2,b}'(\omega)$  data of various PI and PS probes having  $M_2\gg M_1$  collapse onto a master curve, indicating that these chemically different probes exhibit universal CR relaxation mode distribution; see also figure 12 of Watanabe et al. 26 and figure 4 of Sawada et al. 44 Furthermore, at low  $\omega$ , those data are well described by the CR–Rouse model 42 shown with the solid black curve (Fourier transformation of  $G_{CR}(t)$  given below),

for linear probe: 
$$G_{CR}(t) = \frac{\rho v_2 RT}{M_2} \sum_{p=1}^{N_2} \exp\left(-\frac{p^2 t}{\tau_{CR}^{[G]}}\right)$$
 with  $N_2 = M_2/M_e$  (8)

Here,  $\tau_{CR}^{[G]}$  is the longest viscoelastic CR relaxation time, and the second-moment average relaxation time (used in the horizontal axis for the black curve in Figure 5) is given by  $\langle \tau_{CR}^{[G]} \rangle = (\pi^2/15)\tau_{CR}^{[G]}$  in the

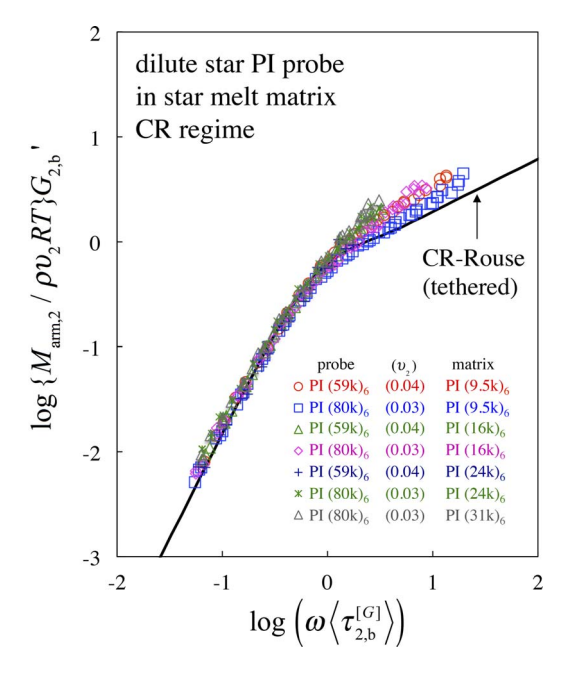


FIG. 6. — Storage modulus  $G_{2,b}'$  of dilute star PI probe entangled only with shorter star PI matrix chains. The  $G_{2,b}'$  data of the probe at 40 °C are normalized by the Rouse factor  $\{M_{arm,2}/\rho v_2 RT\}$  and plotted against the reduced frequency,  $\omega \langle \tau_{2,b}^{[G]} \rangle$ .

Data are taken from Watanabe et al. <sup>36</sup> with permission.

continuous treatment<sup>1</sup> for  $N \gg 1$ . (The numerical pre-factor of  $\pi^2/15$  is obtained from the second line of Eq. 7, with  $G_{2,b}(t)$  therein being replaced by  $G_{CR}(t)$  given by Eq. 8.)

The universality of the mode distribution seen in Figure 5 vanishes when  $M_2$  and  $M_1$  are not sufficiently separated and the CR mechanism does not dominate the probe relaxation; see figure 3 of Sawada et al., <sup>44</sup> figure 4 of Qiao et al., <sup>51</sup> and figure S5 in Supporting Information of Matsumiya et al. <sup>37</sup> Thus, this universality is an important criterion for judging if the probe relaxation is dominated by the CR mechanism.

This criterion can be cast as a critical value of the Struglinski–Graessley parameter  $SG = M_2 M_e^2/M_1^3$ . This SG is defined as a ratio of the reptation time of the probe,  $\tau_{\rm rep,2} \propto M_2^3/M_e$ , to the Rouse-type CR relaxation time of the probe,  $\tau_{\rm CR,2} \propto \tau_{\rm rep,1} \ (M_2/M_e)^2 \propto M_1^3 M_2^2/M_e^3$ , and numerical pre-factors in  $\tau_{\rm rep,2}$  and  $\tau_{\rm CR,2}$  are omitted in SG. (The matrix reptation time  $\tau_{\rm rep,1}$  involved in  $\tau_{\rm CR,2}$  differs from the actual relaxation time of the matrix, as discussed later in relation to Figures 9 and 10.) The universal mode distribution (namely, the CR dominance in the probe relaxation) is experimentally found only in ranges of  $SG \geq 0.2$  and  $SG \geq 0.5$  for PI<sup>44</sup> and PS<sup>1,46–48</sup> probes, respectively. The critical SG value for the CR dominance is smaller for PI than for PS, suggesting that the CR effect on the relaxation emerges more prominently for PI than for PS when CR is competing with other relaxation mechanisms such as reptation. This difference between PI and PS is further discussed later for Figures 9, 11, and 12.

The CR relaxation has been observed also for dilute star PI probes entangled with much shorter matrix star PI chains. <sup>36</sup> Figure 6 shows data of the normalized storage modulus of those star probes,  $\{M_{\text{arm},2}/\rho v_2 RT\}G_{2,b}'(\omega)$  with  $M_{\text{arm},2}$  being the arm molecular weight of the probe, plotted against the reduce frequency  $\omega \langle \tau_{2,b}^{[G]} \rangle$ . The black solid curve indicates the reduced storage modulus obtained from the CR–Rouse relaxation modulus of tethered chains,

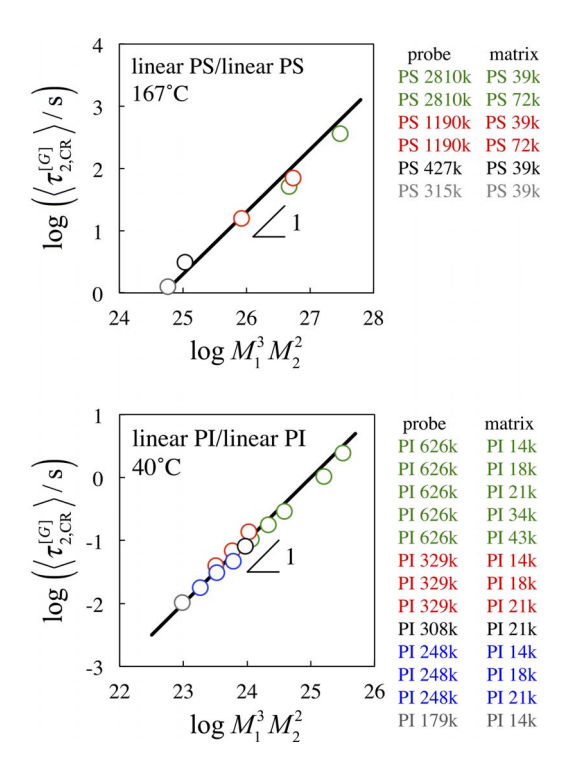


FIG. 7. — Second-moment average viscoelastic CR relaxation time of dilute linear PS and PI probes in much shorter linear PS and PI matrices at 167 and 40 °C, respectively. The plots shown with the same color indicate the relaxation time data obtained for a given probe in different matrices (the matrices are mostly common for different probes), as shown in the legend. Those data are double-logarithmically plotted against  $M_1^3 M_2^2$ . Data are taken from Watanabe et al.  $^{34,44-46}$  with permission.

for star probe: 
$$G_{CR}(t) = \frac{\rho v_2 RT}{M_{arm,2}} \sum_{p=1}^{N_{arm,2}} \exp\left(-\frac{(2p-1)^2 t}{\tau_{CR}^{[G]}}\right)$$
 with  $N_{arm,2} = M_{arm,2}/M_e$  (9)

(The average relaxation time associated with Eq. 9 is given by  $\langle \tau_{\rm CR}^{[G]} \rangle = (\pi^2/12) \tau_{\rm CR}^{[G]}$  for  $N_{\rm arm,2} \gg 1$ , where the pre-factor of  $\pi^2/12$  is obtained from the second line of Eq. 7 with  $G_{2,b}(t)$  therein being replaced by  $G_{\rm CR}(t)$  given by Eq. 9.) The reduced modulus data of the star probes exhibit almost universal dependence on  $\omega \langle \tau_{2,b}^{[G]} \rangle$  at low  $\omega < 2/\langle \tau_{2,b}^{[G]} \rangle$  irrespective of  $M_{1,\rm arm}$  and  $M_{2,\rm arm}$  of the matrix and probe arms, and are close to the CR–Rouse modulus, although deviation from this universal dependence is noted at high  $\omega$  because of fast relaxation of the probe attributable to shallow CLF. It needs to be added that the deviation from the universal  $\omega \langle \tau_{2,b}^{[G]} \rangle$  dependence is not clearly observed for the linear probes (cf. Figure 5), because those linear probes have much higher  $M_2$  compared to the star probe arms tested in Figure 6, and thus the non-universality due to CLF is not clearly resolved at the frequencies examined in Figure 5.

2. Data of CR Relaxation Time. — For the dilute probes exhibiting the universal behavior of  $G_{2,b}'(\omega)$  at low  $\omega$  (cf. Figures 5 and 6), the  $\langle \tau_{2,b}^{[G]} \rangle$  data can be used as the second-moment average viscoelastic CR relaxation time  $\langle \tau_{2,CR}^{[G]} \rangle$ . The  $\langle \tau_{2,CR}^{[G]} \rangle$  data available in the literature are summarized in Figure 7 for various linear probes in various linear matrices  $^{34,44-46}$  and in Figure 8 for two star PI probes in various star PI matrices.  $^{36}$  The plots shown with the same color indicate the  $\langle \tau_{2,CR}^{[G]} \rangle$  data obtained for a given probe in different matrices (and the matrices are mostly common for different probes), as shown in the legend. Those  $\langle \tau_{2,CR}^{[G]} \rangle$  data, cast in

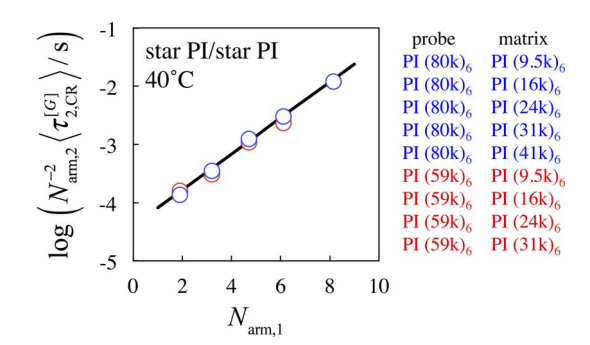


FIG. 8. — Second-moment average viscoelastic CR relaxation time of dilute star PI probes in shorter star PI matrices at 40 °C. The relaxation time data normalized by the CR–Rouse factor for the probe star arm relaxation time  $N_{\rm arm,2}^{-2}$ , with  $N_{\rm arm,2}$  being the number of entanglements per probe arm, are semi-logarithmically plotted against the number of entanglements per matrix star arm,  $N_{\rm arm,1}$ . The plots shown with the same color indicate the relaxation time data obtained for a given probe in different matrices (the matrices are mostly common for the two probes), as shown in the legend. Data are taken from Watanabe et al.  $^{36}$  with permission.

empirical equations shown later, allow us to estimate the CR relaxation time of *monodisperse* linear and star chains in bulk, thereby offering an experimental basis for discussion of the CR contribution to the relaxation of those chains.

In Figure 7, the  $\langle \tau_{2,\text{CR}}^{[G]} \rangle$  data of various linear probes in various linear matrices collapse on a universal line when plotted double-logarithmically against  $M_1{}^3M_2{}^2$ , as noted in the top and bottom panels for PS and PI, respectively. The proportionality to  $M_2^2$  is in accord with the Rouse-like feature of the actual CR process observed for the PI and PS probes (cf. Figure 5). Similarly, for two star PI probes in various star PI matrices, the normalized  $N_{\text{arm},2}^{-2} \langle \tau_{2,\text{CR}}^{[G]} \rangle$  data with  $N_{\text{arm},2}^{-2}$  being the CR-Rouse factor for the probe arm relaxation time collapse on a line when plotted semi-logarithmically against  $N_{\text{arm},1}$ , where  $N_{\text{arm},1}$  and  $N_{\text{arm},2}$  indicate the entanglement number per arm of the probe and matrix star chains, respectively:  $N_{\text{arm},j} = M_{\text{arm},j}/M_e$  with  $M_e = 5.0 \times 10^3$  for PI. (The normalization by the CR-Rouse factor was necessary for collapse of the plots for the two star probes.) These results can be cast in the following empirical equations (shown in Figures 7 and 8 with black lines):

for the linear PS probe in linear PS melt at 167 °C<sup>46</sup>

$$\langle \tau_{2,\text{CR}}^{[G]} \rangle = \frac{\pi^2}{15} \tau_{2,\text{CR}}^{[G]} = 2.0 \times 10^{-25} M_1^3 M_2^2 \text{(in s)}$$
 (10)

for the linear PI probe in linear PI melt at 40  $^{\circ}\mathrm{C}^{44,51}$ 

$$\langle \tau_{2,\text{CR}}^{[G]} \rangle = \frac{\pi^2}{15} \tau_{2,\text{CR}}^{[G]} = 1.0 \times 10^{-25} M_1^3 M_2^2 (\text{in s})$$
 (11)

for the star PI probe in star PI melt at 40 °C<sup>36</sup>

$$\langle \tau_{2,\text{CR}}^{[G]} \rangle = \frac{\pi^2}{12} \tau_{2,\text{CR}}^{[G]} = 4.0 \times 10^{-5} N_{\text{arm},2}^2 \exp\left\{0.71 N_{\text{arm},1}\right\} \text{ (in s)}$$
 (12)

These empirical equations are used in a test of the CR contribution to the terminal relaxation in monodisperse bulk shown below and in an analysis of the DTD process explained later. (The  $\langle \tau_{2,\text{CR}}^{[G]} \rangle$  data of linear probes are well described by those equations, but an equally good description is given by an empirical equation with slightly weaker  $M_1$  dependence. We extend the test and analysis hardly changed even if the latter equation was used. Thus, for definiteness, we adopt Eqs. 10–12 as the empirical equations that serve as the basis of our test/analysis.)

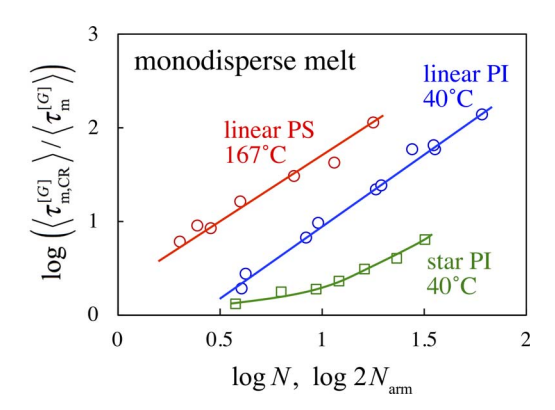


FIG. 9. — Ratio of the second-moment average viscoelastic CR relaxation time  $\langle \tau_{m,CR}^{[G]} \rangle$  to the measured second-moment average relaxation time  $\langle \tau_{m}^{[G]} \rangle$  obtained for monodisperse linear PS and PI and monodisperse star PI melts at temperatures as indicated.  $\langle \tau_{m,CR}^{[G]} \rangle$  was evaluated from the empirical equations (Eqs. 10–12) for the CR time data of dilute probes in much shorter matrices. The  $\langle \tau_{m,CR}^{[G]} \rangle / \langle \tau_{m}^{[G]} \rangle$  ratio for monodisperse linear chains is plotted against the number N of entanglements per chain, and the ratio for monodisperse star chains is plotted against the number  $2N_{arm}$  of entanglements per the longest span (two arms) of the star chain. Data are taken from Watanabe et al.  $^{29,34-36,44-46,51,52}$  with permission.

Setting  $M_1 = M_2 = M$  in Eqs. 10 and 11, we can experimentally evaluate the average viscoelastic CR relaxation time  $\langle \tau_{m,CR}^{[G]} \rangle$  of monodisperse linear PS and PI samples of the molecular weights M. Similarly, from Eq. 12 with  $N_{arm,1} = N_{arm,2} = N_{arm}$ , we obtain  $\langle \tau_{m,CR}^{[G]} \rangle$  of monodisperse star PI samples. For those PS and PI samples, the second-moment average relaxation time (terminal relaxation time)  $\langle \tau_{m,CR}^{[G]} \rangle$  has been obtained as a product of the zero-shear viscosity and recoverable compliance, and thus the  $\langle \tau_{m,CR}^{[G]} \rangle / \langle \tau_{m}^{[G]} \rangle$  ratio can be evaluated in a purely empirical way. Figure 9 compares this ratio for the linear PS and PI as well as for the star PI. The segmental friction involved in  $\langle \tau_{m,CR}^{[G]} \rangle$  and  $\langle \tau_{m}^{[G]} \rangle$  is canceled in the ratio, so that the comparison in Figure 9 allows us to unequivocally examine differences of the CR contribution to the terminal relaxation of respective polymers.

Comparing the monodisperse linear and star PI having the same entanglement number *per chain span*, in other words having  $N=2N_{\rm arm}$  (blue and green symbols in Figure 9), we note that the  $\langle \tau_{\rm m,CR}^{[G]} \rangle / \langle \tau_{\rm m}^{[G]} \rangle$  ratio is considerably smaller and thus the CR contribution to the terminal relaxation is significantly larger for the star PI. This fact is also deduced in our later analysis of the DTD process. (The  $\langle \tau_{\rm m,CR}^{[G]} \rangle / \langle \tau_{\rm m}^{[G]} \rangle$  ratio smaller for the star chain is also expected from the tube model assuming the full dilation of the tube for both linear and star chains, but this model itself fails for the monodisperse star chain, as shown later in that analysis.)

We also note that the  $\langle \tau_{m,CR}^{[G]} \rangle / \langle \tau_{m}^{[G]} \rangle$  ratio is considerably smaller and the CR contribution is considerably larger for linear PI than for linear PS having the same entanglement number N; cf. blue and red symbols. In our ordinary understanding, the terminal viscoelastic relaxation of entangled monodisperse linear polymers is uniquely determined by the plateau modulus  $G_N$  and the terminal relaxation time  $\langle \tau_m^{[G]} \rangle$ . However, the considerable difference of the  $\langle \tau_{m,CR}^{[G]} \rangle / \langle \tau_m^{[G]} \rangle$  ratio noted for linear PI and PS (Figure 9) suggests that this understanding needs to be refined for the CR relaxation of those polymers. This difference is further tested below in relation to the  $M_1$  dependence of the CR time of probes in blends. Readers who like to skip this test can directly proceed to the "D. Experimental Test of Dynamic Tube Dilation Mechanism" section where the DTD mechanism is examined experimentally.

3. Factors Determining CR Relaxation Time. — In the simplest molecular view, the viscoelastic CR relaxation time of a dilute probe,  $\langle \tau_{2,\text{CR}}^{[G]} \rangle$ , is expected to be proportional to the terminal relaxation time of the pure matrix,  $\langle \tau_{1,\text{m}}^{[G]} \rangle$ . However, this is not the case in experiments. For

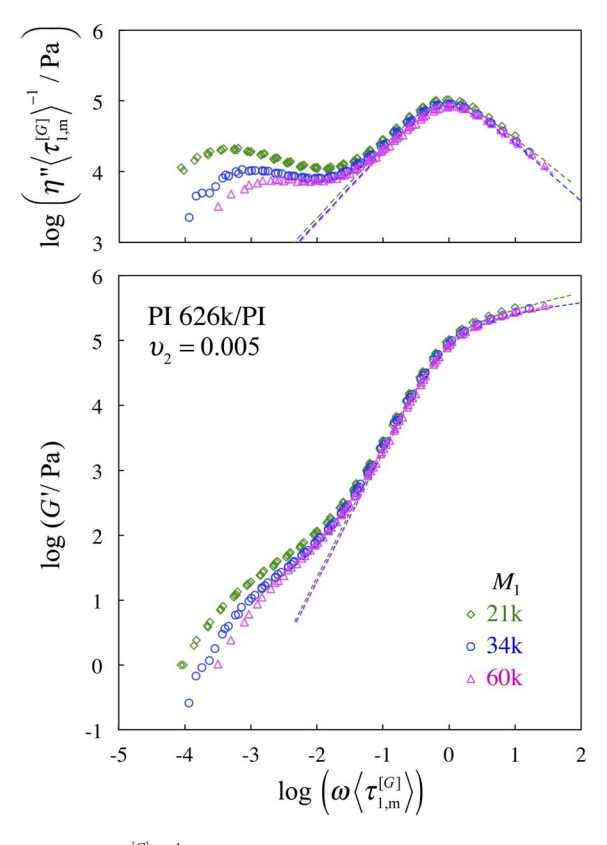


FIG. 10. — Comparison of G' and  $\eta'' \langle \tau_{1,m}^{[G]} \rangle^{-1}$  data of PI 626k/PI blends at 40 °C. The dilute PI 626k probe therein exhibits the CR relaxation. Data are taken from Sawada et al. 44 with permission.

the star PI matrices examined in Figure 6 ( $M_{\rm arm,1} = 9.5 \,\mathrm{k-41k}$ ), the relaxation time is well described by an empirical equation,  $\langle \tau_{1,\mathrm{m}}^{[G]} \rangle = 2.3 \times 10^{-5} N_{\rm arm,1}^2 \,\mathrm{exp}\{0.75 N_{\rm arm,1}\}$  (in s) at 40 °C, with  $N_{\rm arm,1}$  being the entanglement number per matrix star arm. This  $N_{\rm arm,1}$  dependence of  $\langle \tau_{1,\mathrm{m}}^{[G]} \rangle$  is stronger than that of  $\langle \tau_{2,\mathrm{CR}}^{[G]} \rangle$  (Eq. 12). Similarly,  $\langle \tau_{1,\mathrm{m}}^{[G]} \rangle$  of the linear PS and PI matrices is proportional to  $M_1^{3.5}$ , and this  $M_1$  dependence is stronger than that of  $\langle \tau_{2,\mathrm{CR}}^{[G]} \rangle$  (cf. Eqs. 10 and 11). These differences between  $\langle \tau_{2,\mathrm{CR}}^{[G]} \rangle$  and  $\langle \tau_{1,\mathrm{m}}^{[G]} \rangle$  are important in our discussion of the CR mechanism and are further examined below for the raw G' and  $\eta''$  data in order to avoid any small uncertainty in the subtraction and zero- $\omega$  extrapolation made for  $\langle \tau_{2,\mathrm{b}}^{[G]} \rangle$  in Eqs. 6 and 7.

For the PI/PI blends that contain the same, dilute PI 626k probe (exhibiting the CR relaxation) but different linear PI matrices, Figure 10 plots the G' and  $\eta'' \langle \tau_{1,m}^{[G]} \rangle^{-1}$  data against the reduced angular frequency  $\omega \langle \tau_{1,m}^{[G]} \rangle$ , with the matrix relaxation time  $\langle \tau_{1,m}^{[G]} \rangle$  being evaluated as the product of the zero-shear viscosity and recoverable compliance of the matrix. (The  $\eta''$  data are normalized by the matrix relaxation time  $\langle \tau_{1,m}^{[G]} \rangle$ .) The dashed curves show the data of the matrices plotted in the same format.

At high  $\omega$  where the matrix (occupying 99.5% of the blends) dominantly contributes to the blend relaxation, the data of the three blends (symbols) and the three matrices (dashed curves) agree with each other when plotted against  $\omega\langle \tau_{1,m}^{[G]} \rangle$ , as clearly noted in Figure 10. This agreement is consistent with our understanding that the terminal viscoelastic relaxation of monodisperse linear polymer is determined by  $G_N$  (common for the three matrices) and  $\langle \tau_{1,m}^{[G]} \rangle$ : for the blends and matrices, the difference of  $N_1$  has been compensated by plotting the data against  $\omega\langle \tau_{1,m}^{[G]} \rangle$  ( $\sim \omega N_1^{3.5}$ ),

which results in the agreement of the high- $\omega$  data. In contrast, no agreement is noted for the low- $\omega$  data of the blends detecting the CR relaxation of the dilute PI 626k probe. Specifically, in the reduced frequency scale of  $\omega\langle\tau_{1,m}^{[G]}\rangle$ , the probe relaxation is systematically accelerated with increasing  $M_1$ , as clearly noted for both G' and  $\eta''\langle\tau_{1,m}^{[G]}\rangle^{-1}$  data. This result indicates, without any further analysis, that  $\langle\tau_{2,\text{CR}}^{[G]}\rangle$  of the probe is more weakly dependent on  $M_1$  compared to  $\langle\tau_{1,m}^{[G]}\rangle$  of the matrix. The factor of  $M_1^3$  appearing in Eqs. 10 and 11 gives just a quantitative description of this experimental fact.

This  $M_1^3$  dependence of  $\langle \tau_{2,CR}^{[G]} \rangle$  could be due to multiplicity of chains sustaining one entanglement (argued by Klein<sup>53</sup>) combined with the CLF contribution to the CR process, <sup>1</sup> or a very broad crossover in the local CR relaxation on an increase of  $M_1$  ( $>M_e$ ) as argued by Read and coworkers<sup>54</sup> (although the corresponding crossover of  $\langle \tau_{1,m}^{[G]} \rangle$  has not been experimentally resolved for monodisperse matrices). The molecular origin(s) of the  $M_1^3$  dependence of  $\langle \tau_{2,CR}^{[G]} \rangle$  deserves further studies.

In relation to the above test of the  $M_1$  dependence of  $\langle \tau_{2,\text{CR}}^{[G]} \rangle$ , it is also informative to examine the difference of  $\langle \tau_{2,\text{CR}}^{[G]} \rangle$  for chemically different PS and PI probes by focusing on the raw G' and  $\eta''$  data so as to again avoid any small uncertainty in the subtraction and zero- $\omega$  extrapolation (Eqs. 6 and 7). For this purpose, Figure 11 shows the normalized  $G'/G_N$  and  $\eta''G_N^{-1}\langle \tau_{1,\text{m}}^{[G]}\rangle^{-1}$  data for PI and PS blends <sup>44,46</sup> that contain dilute probes in linear matrices of very similar entanglement numbers,  $N_1$ =6.9 and 6.8 for PS 124k and PI 34k in the top panel and  $N_1$ =4.0 and 4.2 for PS 72k and PI 21k in the bottom panel: the normalization by  $G_N$  is necessary for direct comparison of the data of chemically different blends. For PS and PI at 167 and 40 °C, respectively,  $G_N/MPa$ =0.21 and 0.48 and  $G_N$ =1.8 × 10<sup>4</sup> and 5.0 × 10<sup>3</sup>, the latter being used for evaluation of  $G_N$ =1.

At high  $\omega$  where the matrix chains dominantly contribute to the relaxation, the data of the blends (symbols) and matrices (dashed curve) collapse on a universal curve when plotted against the reduced frequency  $\omega\langle \tau_{1,m}^{[G]} \rangle$ , as noted in Figure 11. This collapse is again in harmony with our understanding that the terminal viscoelastic relaxation of monodisperse linear polymers (matrix in this case) is determined by  $G_N$  and  $\langle \tau_{1,m}^{[G]} \rangle$ . However, at low  $\omega$  where the CR relaxation of the dilute probe dominates the blend relaxation, the PS and PI blends exhibit a clear difference in their data.

In Figure 11, the differences in the volume fraction  $v_2$  and the entanglement number  $N_2$  of the probes,  $v_2=0.01$  and  $N_2=156$  for PS 2.8M and  $v_2=0.005$  and  $N_2=125$  for PI 626k, partly contribute to the difference of the low- $\omega$  CR relaxation of these probes. However, this difference due to the differences in  $N_2$  and  $v_2$  can be removed when the G' and  $\eta''\{\langle \tau_{1,m}^{[G]} \rangle N_2^2\}^{-1}$  data are normalized by the Rouse factor for the probe modulus,  $F_R = \{M_2/\rho v_2RT\}$ , and plotted against a reduced frequency  $\omega(\tau_{1,m}^{[G]})N_2^2$ , where  $N_2^2$  is the Rouse factor for the CR time of the probe. However, the difference of the low- $\omega$  CR relaxation of the PI and PS probes clearly remains even after this normalization, as shown in Figure 12. This remaining difference does not vanish even if the normalized  $F_RG'$  and  $F_R\eta''\{\langle \tau_{1,m}^{[G]} \rangle N_2^2\}^{-1}$  data are plotted against another type of reduced frequency,  $\omega N_1^\alpha N_2^\alpha$  with  $\alpha=3$  or 3.5 (because the PS and PI matrices have almost identical  $N_1$ ).

The difference between the PS and PI probes seen in Figure 12 clearly indicates that these probes have different CR relaxation times  $\langle \tau_{2,\text{CR}}^{[G]} \rangle$  even when  $N_1$  and  $N_2$  are common for them. In other words,  $\langle \tau_{2,\text{CR}}^{[G]} \rangle$  is not uniquely determined by  $N_2$  and the matrix relaxation time  $\langle \tau_{1,\text{m}}^{[G]} \rangle$  but is affected by an extra factor that changes with the chemical structure of the chain. This extra factor, not clearly recognized for monodisperse polymers, may correspond to the number z of local constraints per entanglement considered in the CR–Rouse model of Graessley:<sup>42</sup> z reflects the number of matrix chains forming an entanglement for the probe chain. If the entanglement is exclusively due to the binary (pair-wise) constraint between the chains irrespective of their chemical structure, the above difference between the PS and PI probes may not be straightforwardly deduced within the CR–Rouse model. A correlation between the extra factor and the chemical structure of the chain is closely related to the nature of entanglement (binary or multiple-chain

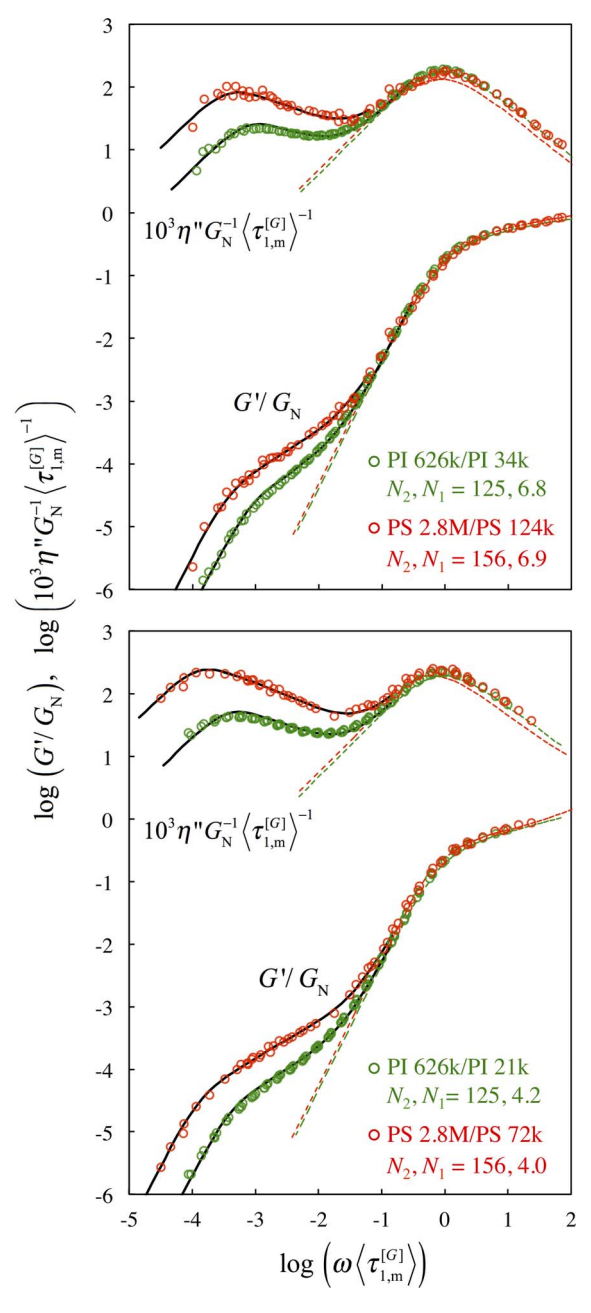


FIG. 11. — Plots of normalized  $G'/G_N$  and  $\eta''G_N^{-1}\langle \tau_{1,m}^{[G]}\rangle^{-1}$  data of PI 626k/PI and PS 2.8M/PS blends (at 40 and 167 °C, respectively) against the reduced frequency  $\omega\langle \tau_{1,m}^{[G]}\rangle$ . The dilute PI 626k and PS 2.8M linear probes ( $\upsilon_2$ =0.005 and 0.01) exhibit CR relaxation. Black curves for  $G'/G_N$  indicate a sum of  $G'_{2,CR}/G_N$  for the CR–Rouse relaxation of the probe (with  $G'_{2,CR}$  being given as Fourier transformation of Eq. 8) and the terminal tail of the  $\upsilon_1 G'_{1,m}/G_N$  data of the matrix. The corresponding sum for  $\eta''G_N^{-1}\langle \tau_{1,m}^{[G]}\rangle^{-1}$  is also shown with the black curves. Data are taken from Watanabe et al. <sup>44,46</sup> with permission.

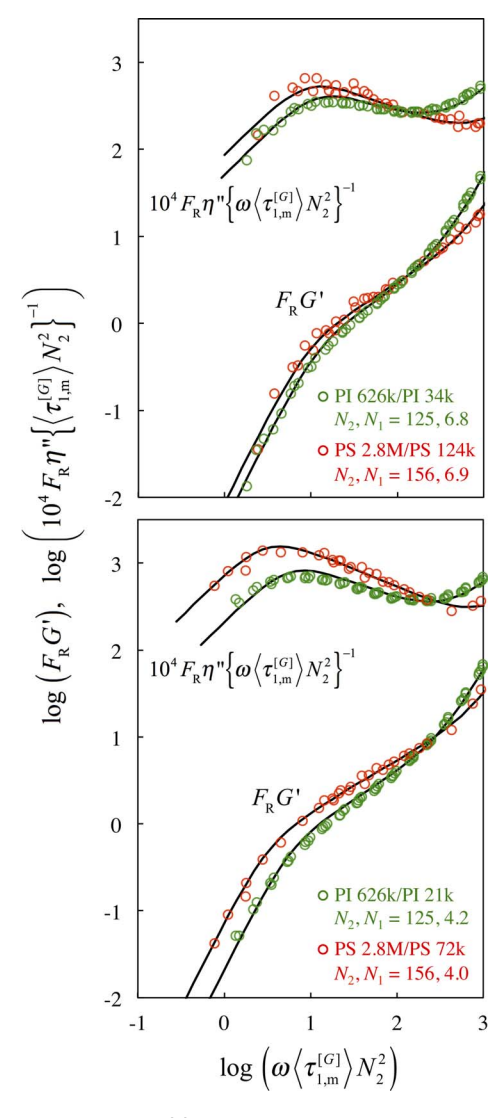


FIG. 12. — Plots of normalized  $F_RG'$  and  $F_R\eta''\{\langle \tau_{1,m}^{[G]} \rangle N_2^2\}^{-1}$  data of PI 626k/PI and PS 2.8M/PS blends examined in Figure 11 against a reduced frequency  $\omega \langle \tau_{1,m}^{[G]} \rangle N_2^2$ . Black curves are the same as those in Figure 11. Data are taken from Watanabe et al. <sup>44,46</sup> with permission.

constraint) and is further discussed later in the "F. Comments on Recent Theoretical Model/Analysis" section in relation to the tube dilation exponent.

Here, it should be emphasized that the extra factor discussed above is absorbed in the numerical front factors in Eqs. 10 and 11, and thus the CR behavior of chemically different PS and PI probes is still described commonly by the CR–Rouse model (with its  $\tau_{\rm CR}^{[G]}$  being specified by Eqs. 10 and 11). In fact, the CR relaxation of the PS 2.8M and PI 626k probes examined in Figures 11 and 12 exhibits the same, Rouse-type mode distribution, as noted from the agreement of the data and black solid curves, where the curves for G' represent a sum of  $G_{\rm CR}'$  of the probe (obtained from  $G_{\rm CR}(t)$  shown in Eq. 8) and the terminal tail of the  $\upsilon_1 G_{1,{\rm m}'}$  data  $(\propto \omega^2)$  of the matrix, and the curves for  $\eta''$ , the corresponding sum reduced by  $\omega$ . Note that the difference between the PS 2.8M and PI 626k probes

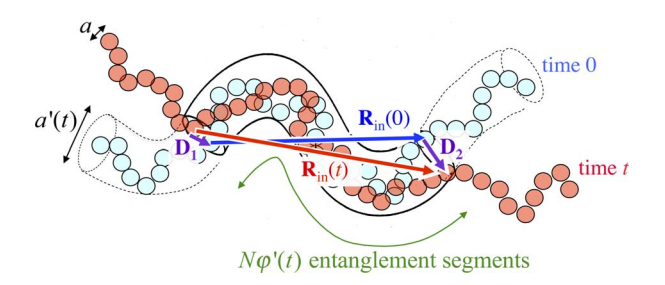


FIG. 13. — Schematic illustration of a dilated tube and a linear chain trapped in it.

in Figures 11 and 12 vanishes when their  $G_{2,b}$  data are normalized by the Rouse factor and plotted against the frequency normalized by their CR time data  $\langle \tau_{2,b}^{[G]} \rangle$ ; see collapse of the plots for those probes around the Rouse–CR curve in Figure 5 (the filled gray square and circle for the PS 2.8M probe in PS 72k and PS 124k matrices, and the unfilled red square and circle for the PI 626k probe in PI 21k and PI 34k matrices). This collapse again indicates the validity of the CR–Rouse model. Thus, in the following sections, we use this model to examine some details of the dynamic tube dilation (DTD) mechanism.

#### D. EXPERIMENTAL TEST OF DYNAMIC TUBE DILATION MECHANISM

The CR-Rouse process has been experimentally confirmed for dilute probes entangled with much shorter matrix chains (cf. Figures 4–6). Thus, the relaxation mechanisms assumed in the fixed entanglement environment, the reptation and arm retraction mechanisms for the linear and star chains (Figure 2), should be modified by the CR mechanism in actual entangled systems. This modification can be made in the time evolution equation of the spatial position of the entanglement segment (subchain explained for Figure 1), as done in the Graham–Likhtman–McLeish–Milner model<sup>55</sup> (for non-linear rheology), for example. However, a combination of the dielectric and viscoelastic data of type-A polymer, PI, enables us to make this modification in a simple and experimental way. This section focuses on this modification. The results presented below are believed to be general and applicable to PS and other amorphous polymers having no type-A dipoles.

As a starting point of the modification, we consider accumulation of the local CR processes that allows successive entanglement segments, say  $\beta(t)$  segments, to be mutually equilibrated through exchange of their positions, thereby behaving as a dilated segment as a whole. This dilated segment serves as a stress-sustaining unit in the time scale of the mutual equilibration. In the tube model, this mutual equilibration is described as the dynamic tube dilation (DTD) illustrated in Figure 2, and the diameter a'(t) of the dilated tube is related to  $\beta(t)$  and the entanglement length a as

$$a'(t) = \{\beta(t)\}^{1/2}a\tag{13}$$

In a short time scale of intrinsic Rouse relaxation within the entanglement segment,  $\beta(t) = 1$  and  $\alpha'(t) = a$ . In a longer time scale,  $\alpha'(t)$  and  $\beta(t)$  increase with t in a manner explained later.

In a given time scale, a chain is equilibrated only up to the length scale of a'(t) and thus topologically constrained in the dilated tube having the diameter a'(t). In that time scale, the chain is allowed to move only in this dilated tube. Namely, the reptation and arm retraction mechanisms for the linear and star chains still work, but these mechanisms need to be redefined with respect to the dilated tube. Figure 13 illustrates this situation for a linear chain. At a time t, portions of the linear chain near its ends have random orientation to lose its memory of the initial orientation. The

remaining portion, having a fraction  $\varphi'(t)$ , is trapped in the dilated tube and preserves its initial orientation (at time 0) defined for every  $\beta(t)$  entanglement segments, thereby contributing to the stress. The situation is the same also for a star chain. Thus, for both linear and star chains, the normalized viscoelastic relaxation function is expressed in terms of  $\beta(t)$  and the survival fraction of the dilated tube,  $\varphi'(t)$ , as<sup>24,35,36,43,51</sup>

$$\mu(t) = \varphi'(t)/\beta(t) \text{ (for both linear and star chains)}$$
 (14)

Equation 14 is equivalent to Eq. 4 in the fixed tube model, except that the dilated segments serve as the stress-sustaining unit and thus the modulus in Eq. 14 exhibits an extra decay by the factor of  $1/\beta(t)$ .

The normalized dielectric relaxation function  $\Phi(t)$  also can be expressed in terms of  $\beta(t)$  and  $\phi'(t)$  with the aid of Figure 13. The dielectric memory of the linear chain is preserved only in the inner portion of the chain shown therein, so that Eq. 3 gives an expression of  $\Phi(t)$  in terms of the end-to-end vector  $\mathbf{R}_{in}$  of that portion,  $\Phi(t) = \langle \mathbf{R}_{in}(t) \cdot \mathbf{R}_{in}(0) \rangle_{eq} / Na^2$ .  $\mathbf{R}_{in}(t)$  at time t is close but not identical to  $\mathbf{R}_{in}(0)$  at time 0 because of the displacement of the inner portion within the edges of the surviving part of the dilated tube; see purple arrows in Figure 13. Because  $\mathbf{R}_{in}(t) = \mathbf{R}_{in}(0) + \mathbf{D}_1 + \mathbf{D}_2$ , with  $\mathbf{D}_1$  and  $\mathbf{D}_2$  being the displacement vectors in those edges, we find  $\Phi(t) = \{\langle \mathbf{R}_{in}(0)^2 \rangle_{eq} + \langle (\mathbf{D}_1 + \mathbf{D}_2) \cdot \mathbf{R}_{in}(0) \rangle_{eq} \} / Na^2 = \{N\phi'(t)a^2 + \langle (\mathbf{D}_1 + \mathbf{D}_2) \cdot \mathbf{R}_{in}(0) \rangle_{eq} \} / Na^2$ . (Note that the surviving part of the dilated tube constrains  $N\phi'(t)$  entanglement segments, and thus  $\langle \mathbf{R}_{in}(0)^2 \rangle_{eq} = N\phi'(t)a^2$ .) Furthermore, considering the Gaussian conformation of the inner portion at equilibrium (where Eq. 3 is defined), we find a relationship  $2\langle (\mathbf{D}_1 + \mathbf{D}_2) \cdot \mathbf{R}_{in}(0) \rangle_{eq} + \langle \mathbf{D}_1^2 \rangle + \langle \mathbf{D}_2^2 \rangle = 0$ , where a relationship valid for the CR–Rouse process,  $^{56} |\langle \mathbf{D}_1^2 \rangle + \langle \mathbf{D}_2^2 \rangle| \gg 2|\langle \mathbf{D}_1 \cdot \mathbf{D}_2 \rangle|$  at  $t < \tau_{CR}^{[G]}$ , has been used. From this relationship and a simple estimate  $^{34} \langle \mathbf{D}^2 \rangle = \{a'(t) - a\}^2/4$ , the above expression of  $\Phi(t)$  is finally rewritten as

$$\Phi(t) = \varphi'(t) - \frac{1}{4N} \left[ \left\{ \beta(t) \right\}^{1/2} - 1 \right]^2 \text{ (for monodisperse linear chain)}^{24,35}$$
 (15)

From a similar analysis, we find an expression of  $\Phi(t)$  of the star chain,

$$\Phi(t) = \varphi'(t) - \frac{1}{8N_{\text{arm}}} \left[ \{\beta(t)\}^{1/2} - 1 \right]^2 \text{ (for monodisperse star chain)}^{33,36}$$
 (16)

The second terms of Eqs. 15 and 16 are a correction due to the displacement in the edges of the surviving part of the dilated tube, but this correction is minor unless the tube is largely dilated to have  $a'(t) \cong \langle \mathbf{R}^2 \rangle_{\rm eq}^{1/2}$ . Thus,  $\Phi(t)$  is close to  $\Phi(t)$  for both linear and star chains, which is similar to the situation in the absence of CR/DTD; cf. Eq. 4. (For monodisperse linear and star PI, respectively,  $\Phi(t)$  and  $\Phi(t)$  are directly compared in figure S2 of Supporting Information of Matsumiya et al.<sup>37</sup> and in figure 9 of Watanabe et al.<sup>36</sup>). Consequently, the relationship between  $\Phi(t)$  and  $\Phi'(t)$  is rather insensitive to the CR and DTD mechanisms. This feature of the dielectric  $\Phi(t)$  makes a sharp contrast to the CR/DTD-sensitivity of the viscoelastic  $\mu(t)$  noted from the factor  $\beta(t)$  in Eq. 14.

This difference between  $\Phi(t)$  and  $\mu(t)$  is very useful for an experimental test of the DTD mechanism. Specifically, we can evaluate the survival fraction  $\varphi'(t)$  of the dilated tube from the dielectric  $\Phi(t)$  data (cf. Eqs. 15 and 16) given that the number of equilibrated entanglement segments  $\beta(t)$  is known. Using these  $\varphi'(t)$  and  $\beta(t)$  in Eq. 14, we can calculate the viscoelastic  $\mu(t)$  expected for the DTD process. Comparison of this calculation with the  $\mu(t)$  data allows us to test whether the molecular picture of DTD can *consistently* describe the  $\Phi(t)$  and  $\mu(t)$  data. This experimental test of the DTD mechanism just focuses on the consistency between  $\Phi(t)$  and  $\mu(t)$  so that it is free from delicate assumptions in detailed model calculation of the t dependence of  $\Phi(t)$  and  $\mu(t)$ . The results of the test are summarized below.

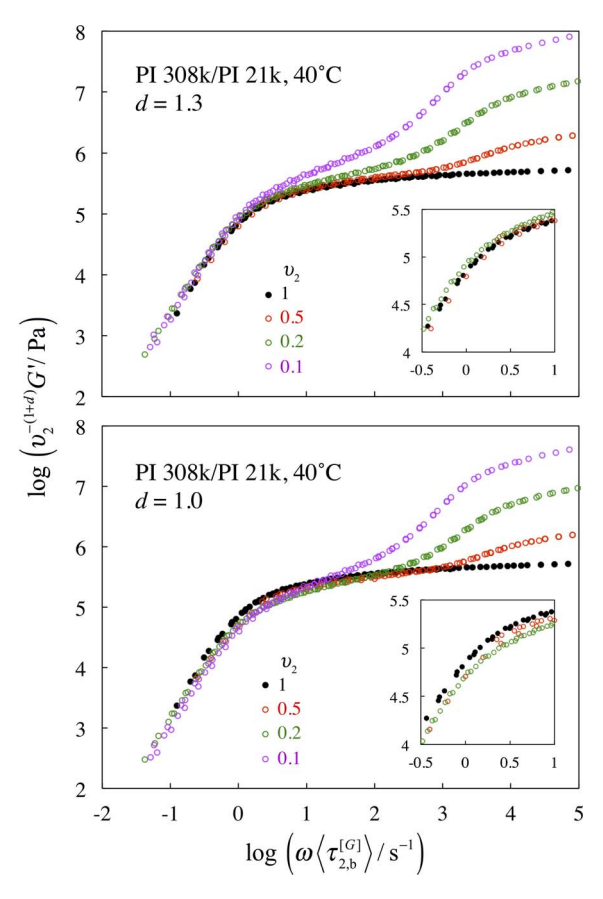


FIG. 14. — G' data of PI 308k/PI 21k blends normalized by a factor of  $v_2^{-(1+d)}$  with d=1.3 (top panel) and d=1.0 (bottom panel). The normalized data are plotted against the normalized frequency,  $\omega \langle \tau_{2,b}^{[G]} \rangle$ . Data are taken from Watanabe et al. <sup>34</sup> with permission

1. Test of Molecular Picture of Full-DTD. — Several molecular models  $^{43,57-59}$  assume that the relaxed portion of the chain behaves as a solvent not contributing to the entanglement, and thus the tube diameter in a melt is fully dilated to the diameter in a solution having a polymer volume fraction  $v = \varphi'(t)$ . With this full-DTD assumption, the number of equilibrated entanglement segments,  $\beta(t)$ , is related to  $\varphi'(t)$  as  $^{24,33,34,43}$ 

$$\beta_{f-DTD}(t) = {\{\phi'(t)\}}^{-d} \text{ with } d = 1.3 \text{ for PI}$$
 (17)

Equation 17 is equivalent to the scaling of the plateau modulus of the solution,  $G_{N,\text{soln}} = G_{N,\text{bulk}} v^{1+d}$ .

The value of the dilation exponent d is a subject of recent theoretical analyses  $^{60,61}$  (that prefer d=1 at short t), as explained later in detail. However, in our experimental test of the molecular picture of full-DTD, d is to be determined directly from the modulus data of blends containing the long chains that are entangled among themselves and with much shorter chains. The G' data of PI 308k/PI 21k blends  $^{34}$  with  $v_2 \ge 0.1$  serve this purpose; the long chains therein (PI 308k) are entangled among themselves as well as with the short chains (PI 21k). In Figure 14, the G' data of those blends are normalized by a factor of  $v_2^{-(1+d)}$  with d=1.3 (top panel) and d=1.0 (bottom panel) and plotted against the normalized frequency  $\omega \langle \tau_{2,b}^{[G]} \rangle$ . Here,  $\langle \tau_{2,b}^{[G]} \rangle$  is the second-moment average viscoelastic

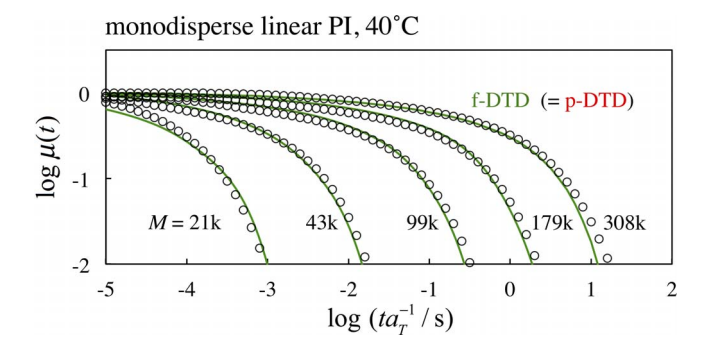


FIG. 15. — Comparison of normalized relaxation modulus  $\mu(t)$  of monodisperse linear PI (circles) with dielectrically evaluated full-DTD modulus  $\mu_{f\text{-DTD}}(t)$  (curves). For monodisperse linear PI,  $\mu_{f\text{-DTD}}(t)$  agrees with the partial-DTD modulus  $\mu_{g\text{-DTD}}(t)$ .  $G^*(\omega)$  data of linear PI reported in Watanabe et al.  $^{34,37}$  were converted into  $\mu(t)$ .

relaxation time of the long chain in the blend evaluated by Eqs. 6 and 7, except that  $G_{1,m}^*(\omega)$  in Eq. 6 is replaced by  $G_{1,m}^*(\lambda\omega)$  where the factor  $\lambda$  represents minor retardation of the matrix relaxation due to the entanglement with the concentrated long chains. <sup>34</sup> (This entanglement suppresses CR for the short matrix chains in the blends to retard their relaxation compared to that in the pure matrix.)

For d=1.3, the  $v_2^{-(1+d)}G'$  data of the PI 308k/PI 21k blends are well superposed on the G' data of bulk PI 308k (black circles) in the terminal relaxation regime at  $\omega \langle \tau_{2,b}^{[G]} \rangle < 2$ , as noted in the top panel of Figure 14. In contrast, the bottom panel shows that d=1.0 gives much poorer superposition, as most clearly noted from comparison of the insets in the top and bottom panels. The corresponding difference, good and poor superposition for d=1.3 and 1.0, is noted also for the  $v_2^{-(1+d)}G''$  data of the blends as well as for the  $v_2^{-(1+d)}G^*$  data of PI 308k solutions in an oligomeric butadiene. <sup>34</sup> Thus, our experimental test of the full-DTD picture adopts d=1.3, as already shown in Eq. 17.

Substituting Eq. 17 into Eqs. 15 and 16, we can use the dielectric  $\Phi(t)$  data of monodisperse linear and star PI to evaluate their  $\varphi'(t)$  for the case of full-DTD. The viscoelastic relaxation function obtained from this  $\varphi'(t)$ ,  $\mu_{\text{f-DTD}}(t) = {\{\varphi'(t)\}}^{1+d}$  with d=1.3 (cf. Eqs. 14 and 17), is shown in Figures 15 and 16 with green curves for comparison with the  $\mu(t)$  data of monodisperse linear  $^{34,37}$  and star PI,  $^{51}$  respectively. (For this comparison, the  $G^*(\omega)$  data of linear PI reported in Watanabe et al.  $^{34,37}$  were converted into  $\mu(t)$ .)

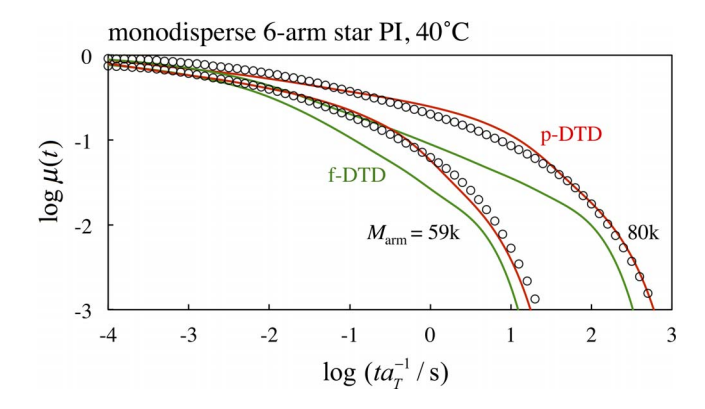


FIG. 16. — Comparison of normalized relaxation modulus  $\mu(t)$  of monodisperse six-arm star PI (circles) with dielectrically evaluated full-DTD modulus  $\mu_{f\text{-DTD}}(t)$  and partial-DTD modulus  $\mu_{p\text{-DTD}}(t)$  (green and red curves). Data are taken from Qiao et al.  $^{51}$  with permission.

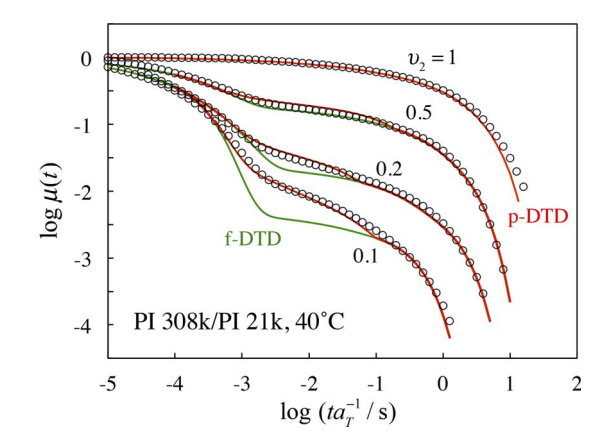


FIG. 17. — Comparison of normalized relaxation modulus  $\mu(t)$  of PI 308k/PI 21k blends (circles) with dielectrically evaluated full-DTD modulus  $\mu_{f\text{-DTD}}(t)$  and partial-DTD modulus  $\mu_{p\text{-DTD}}(t)$  (green and red curves). Data for  $\upsilon_2 = 0.1 - 0.5$  are taken from Watanabe et al. <sup>34,35</sup> with permission, and the data for  $\upsilon_2 = 1.0$  from Figure 15.

For the PI 308k/PI 21k blends examined in Figure 14, we first need to decompose the  $\Phi(t)$  data of the blend as a whole into contributions  $\Phi_1(t)$  and  $\Phi_2(t)$  of the short and long linear chains (components 1 and 2):<sup>34</sup>  $\Phi(t) = (1 - v_2)\Phi_1(t) + v_2\Phi_2(t)$ . The mode distribution of  $\Phi_1(t)$  was found to agree well with that of the short chain in monodisperse bulk, <sup>34</sup> which enabled easy decomposition. Then, from those  $\Phi_j(t)$ ,  $\varphi_j'(t)$  of the component j was evaluated through a relationship analogous to Eq. 15 combined with Eq. 17,  $\Phi_j(t) = \varphi_j'(t) - (1/4N_j)[\{\varphi'(t)\}^{-d/2} - 1]^2$  with j = 1,2 and  $\varphi'(t) = (1 - v_2)\varphi_1'(t) + v_2\varphi_2'(t)$ . <sup>34</sup> (This relationship considers the dilated tube diameter to be common for the long and short chains, as noted for the factor in the second term,  $\{\varphi'(t)\}^{-d/2} = a_{f-DTD}'(t)/a$  for full-DTD.) The corresponding viscoelastic relaxation function,  $\mu_{f-DTD}(t) = \{\varphi'(t)\}^{1+d}$  with d = 1.3, is compared with the  $\mu(t)$  data in Figures 17.<sup>34</sup>

For the monodisperse linear PI chains (Figure 15),  $\mu_{f\text{-DTD}}(t)$  (green curves) is in good agreement with the  $\mu(t)$  data (circles) in the entire range of t. Thus, the full-DTD assumption is valid for consistently describing the  $\Phi(t)$  and  $\mu(t)$  data of those chains. This validity has been confirmed also for  $G'(\omega)$  and  $G''(\omega)$  data in the frequency domain (see figure S1 in Supporting Information of Matsumiya et al.<sup>37</sup>).

In contrast, for the monodisperse star PI (Figure 16) as well as for the blends of linear PI (Figure 17),  $\mu_{f\text{-DTD}}(t)$  (green curves) is considerably smaller than the  $\mu(t)$  data at intermediate t. Namely, the molecular picture of full-DTD significantly overestimates the viscoelastic relaxation at those t, as noted also in the frequency domain. <sup>33,34</sup> (Similar results have been found also for a Cayley-tree type branched PI. <sup>56</sup>) In particular, for the blends with a small volume fraction of the long chain ( $\nu_2$ =0.1 and 0.2), this overestimation is most significant at  $t = 10^{-3}$ – $10^{-1}$  s where the short matrix chain (majority in the blends) has fully relaxed but the long chain has not; see Figure 17. Nevertheless, at either longer or shorter time scales,  $\mu_{f\text{-DTD}}(t)$  agrees with the  $\mu(t)$  data of the blends. These results suggest the origin of the failure of the full-DTD picture, as discussed in the following section.

Here, it is informative to examine the prediction of the Milner–McLeish (MM) model<sup>58</sup> for entangled monodisperse star chains. The MM model is a sophisticated tube model that incorporates the stochastic, first-passage nature of the arm retraction but still adopts the full-DTD picture. The normalized viscoelastic and dielectric relaxation functions of this model can be summarized as<sup>33,58</sup>

$$\mu(t) = \frac{1+d}{L_{\text{eq}}} \int_0^{L_{\text{eq}}} \left\{ 1 - \frac{z}{L_{\text{eq}}} \right\}^d \exp\left(-\frac{t}{\tau_{\text{MM}}(z)}\right) dz$$
 (18)

and

$$\Phi(t) = \frac{1}{KL_{\text{eq}}} \int_0^{L_{\text{eq}} - a} \left\{ 1 + \Xi(z) \right\} \exp\left(-\frac{t}{\tau_{\text{MM}}(z)}\right) dz$$
 (19a)

with

$$K = 1 - \frac{a}{L_{\text{eq}}} + \frac{1}{8N_{\text{arm}}} \left\{ 1 - \left(\frac{a}{L_{\text{eq}}}\right)^{-d/2} \right\}^2$$
 (19b)

$$\Xi(z) = \frac{d}{8N_{\rm arm}} \left\{ \left( 1 - \frac{z}{L_{\rm eq}} \right)^{-(1+d)} - \left( 1 - \frac{z}{L_{\rm eq}} \right)^{-(1+d/2)} \right\}$$
 (19c)

In Eqs. 18 and 19,  $L_{eq} = N_{arm}a$  is the equilibrium contour length of the star arm consisting of  $N_{arm}$ entanglement segments,  $\tau_{MM}(z)$  is a time required for the arm retraction over a contour length z (that includes both shallow and deep retraction, the latter being associated with an entropic penalty), and d is the dilation exponent. Figure 18 compares the MM calculation (with d=1.3) and the  $\mu(t)$  and  $\Phi(t)$  data of six-arm star PI (80k)<sub>6</sub> sample. (The data and calculation in the frequency domain published in Watanabe et al.<sup>33</sup> were converted into the time domain.) For an adequate choice of the model parameters, the MM model excellently describes the  $\mu(t)$  data; see red curve in the top panel. However, the model with the same parameters gives the dielectric  $\Phi(t)$ considerably larger than the data at long t, as shown with the red curve in the bottom panel. An adjustment of the parameters allows the MM model to describe the  $\Phi(t)$  data (cf. green curve in the bottom panel), but the viscoelastic  $\mu(t)$  calculated with those adjusted parameters (green curve in the top panel) is significantly smaller than the data. Namely, even the sophisticated tube model fails to consistently describe the viscoelastic and dielectric data of star PI, given that the model adopts the full-DTD picture. (The failure is noted also for the model calculation with d=1.) This result for the MM model is consistent with the results of experimental test of the full-DTD picture presented in Figure 16: the MM fitting of the  $\Phi(t)$  data gives  $\mu(t)$  being smaller than observed (cf. green curve in top panel of Figure 18), which is similar to the experimental results seen in Figure 16.

2. Test of Molecular Picture of Partial-DTD. — The local CR process is accumulated during the relaxation to expand a length scale of lateral displacement allowed for the entanglement segments. DTD is the molecular picture that makes coarse-graining of this accumulation in both length and time scales to define an effectively dilated tube in a given time scale. Thus, the DTD picture should be valid if the length and time scales are consistently coarse-grained. For a test of this consistency, the number of equilibrated entanglement segments assumed in the full-DTD picture,  $\beta_{\text{f-DTD}}(t) = \{\phi'(t)\}^{-d}$  (Eq. 17), should be compared with the maximum number of equilibrated segments allowed by the CR mechanism,  $\beta_{\text{CR}}(t) = 1/\psi_{\text{CR}}(t)$ , with  $\psi_{\text{CR}}(t)$  being a survival function specified below.

For a monodisperse linear chain composed of N entanglement segments,  $\psi_{CR}(t)$  can be expressed as  $^{36,51}$ 

for monodisperse linear chain

$$\psi_{\mathrm{CR}}(t) = \frac{1}{N} \left\{ \sum_{p=1}^{N-N_{\mathrm{CLF}}} \exp\left(-\frac{r_{p}^{[\mathrm{CR,linear}]}}{\tau_{\mathrm{CR}}}t\right) + \sum_{p=1}^{N_{\mathrm{CLF}}} \exp\left(-\frac{r_{p}^{[\mathrm{CLF,linear}]}}{\tau_{\mathrm{CLF}}}t\right) \right\}$$
(20)

with

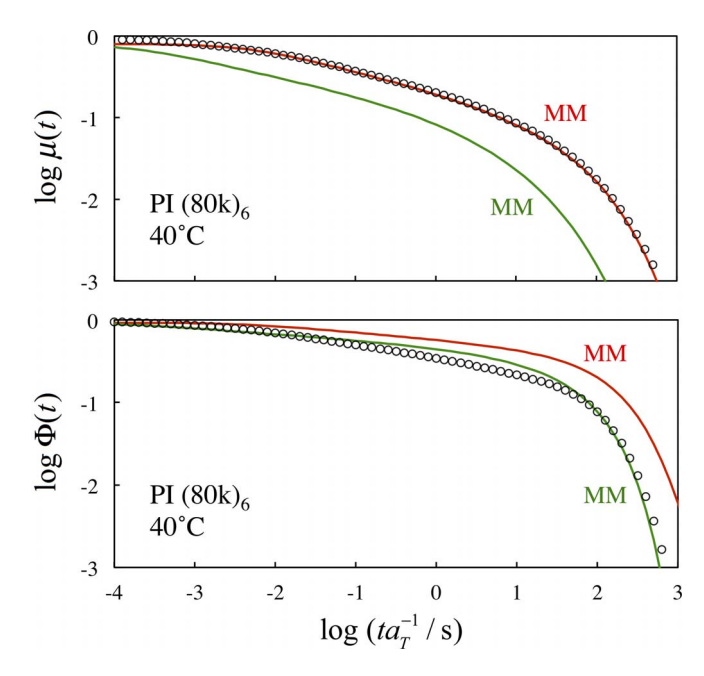


FIG. 18. — Test of full-DTD model (Milner-McLeish model) for viscoelastic and dielectric relaxation functions,  $\mu(t)$  and  $\Phi(t)$ , of monodisperse star PI (80k)<sub>6</sub>. The model parameters are common for  $\mu(t)$  and  $\Phi(t)$  (but differ for the red and green curves). For further detail, see text. Data and calculation in the frequency domain<sup>33</sup> were converted into the time domain.

$$r_p^{\text{[CR,linear]}} = \sin^2\left(\frac{p\pi}{2N}\right)\sin^{-2}\left(\frac{\pi}{2N}\right)$$
 (21a)

and

$$r_p^{\text{[CLF,linear]}} = \sin^2\left(\frac{p\pi}{2N_{\text{CLF}}}\right)\sin^{-2}\left(\frac{\pi}{2N_{\text{CLF}}}\right), N_{\text{CLF}} = \sqrt{N}$$
 (21b)

Here,  $\tau_{\rm CR}$  denotes the CR time defined for the displacement of entanglement segments and is equivalent to the known dielectric CR time for the end-to-end fluctuation,  $\tau_{\rm CR}^{[\varepsilon]} = 2\tau_{\rm CR}^{[G]}$  ( $\tau_{\rm CR}^{[\varepsilon]}$  has been confirmed to coincide with  $2\tau_{\rm CR}^{[G]}$  for dilute PI probes in the CR regime<sup>34</sup>). Equation 20 considers the CR–Rouse process of a given chain (probe) activated by the global motion of the surrounding chains (the first summation in Eq. 20) and by the contour length fluctuation (CLF) of the probe (equivalent to the surrounding chains in the monodisperse system; the second summation).  $N_{\rm CLF}$  is the number of entanglement segments relaxing through CLF that occurs with a known characteristic time  $\tau_{\rm CLF}$  (intrinsic Rouse time of the whole chain backbone). The factor  $r_p^{[{\rm CR},{\rm linear}]}$  indicates a relaxation time ratio of p-th CR mode to the slowest CR mode, and the other factor  $r_p^{[{\rm CLF},{\rm linear}]}$ , the ratio for p-th and slowest CLF modes. (For high-M linear PI, the CLF term in Eq. 20 is not important at long t. Thus, Eq. 20 with  $N_{\rm CLF}$ =0 was used in Watanabe et al. <sup>35</sup> However, for completeness, Eq. 20 with  $N_{\rm CLF} = \sqrt{N}$  was used in this article to evaluate  $\psi_{\rm CR}(t)$  for monodisperse linear PI examined in Figure 15.)

For the star chain having  $N_{\text{arm}}$  entanglement segments per arm,  $\psi_{\text{CR}}(t)$  is also given by Eqs. 20 and 21, where N is replaced by  $N_{\text{arm}}$  and the relaxation time ratios,  $r_p$ , by the Rouse-type ratios for a tethered chain,  $^{36,51}$ 

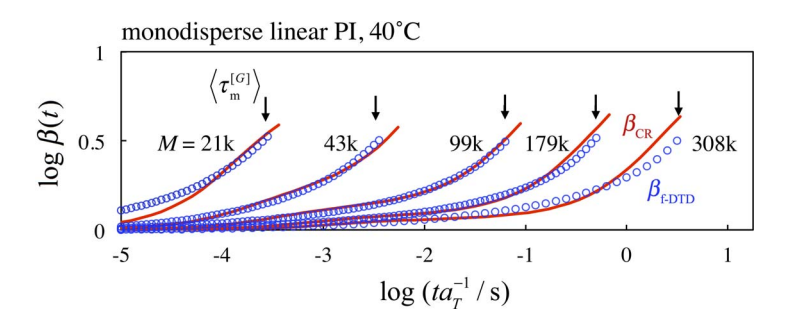


FIG. 19. — Equilibration number of entanglement segments of monodisperse linear PI assumed in the full-DTD molecular picture,  $\beta_{\text{f-DTD}}(t)$  (blue circles). The maximum equilibration number allowed by the CR–Rouse mechanism,  $\beta_{\text{CR}}(t)$  evaluated in this article (cf. Eqs. 20 and 21), is shown with red curves.  $\beta_{\text{f-DTD}}(t)$  data are taken from Watanabe et al.<sup>35</sup> and Supporting Information of Matsumiya et al.<sup>37</sup> with permission.

$$r_p^{[CR,star]} = \sin^2\left(\frac{\{2p-1\}\pi}{2\{2N_{arm}+1\}}\right)\sin^{-2}\left(\frac{\pi}{2\{2N_{arm}+1\}}\right)$$
 (22a)

$$r_p^{[\text{CLF,star}]} = \sin^2 \left( \frac{\{2p-1\}\pi}{2\{2N_{\text{CLF}}+1\}} \right) \sin^{-2} \left( \frac{\pi}{2\{2N_{\text{CLF}}+1\}} \right), \ N_{\text{CLF}} = \sqrt{N_{\text{arm}}}$$
 (22b)

The tube model generally assumes that the branching point of the star chain is fixed in space until the star arm fully relaxes, which leads to the use of  $r_p$  for the tethered chain in Eq. 22.

Here, a comment needs to be made for the dilute linear probes examined in Figure 5. In principle, the CLF contribution specified above also needs to be considered for these probes. However, all those probes have large  $N_2$  ( $\geq 24$ ), so that their relaxation at  $\omega \langle \tau_{2,b}^{[G]} \rangle \leq 100$  (examined in Figure 5) is dominated by the low-order CR–Rouse modes with the index up to  $p \cong 10$  and is negligibly contributed from the fast CLF modes. For this reason, those linear probes exhibit the universal terminal relaxation that coincides with the CR–Rouse relaxation (solid curve in Figure 5). (At low  $\omega \langle \tau_{2,b}^{[G]} \rangle \leq 100$ ,  $\mu(t) = \phi'(t)/\beta_{\rm CR}(t) = \phi'(t)\psi_{\rm CR}(t)$  evaluated on the basis of Eqs. 14 and 20 is numerically indistinguishable from a reduced modulus  $\{M_2/N_2\rho v_2RT\}G_{\rm CR}(t)$ , with  $G_{\rm CR}(t)$  being given by Eq. 8.) The situation is a little different for the star probes examined in Figure 6. Those star probes have just moderately large  $N_{\rm arm}$  (=12 and 16), and their terminal relaxation is non-negligibly contributed from the CLF modes. Because of this CLF contribution, the star probes exhibit less universal terminal relaxation compared to the linear probes (cf. Figures 5 and 6), as explained earlier.

Now, we compare  $\beta_{\text{f-DTD}}(t)$  and  $\beta_{\text{CR}}(t)$  (=  $1/\psi_{\text{CR}}(t)$ ) for the monodisperse linear and star chains examined in Figures 15 and 16. ( $\mu_{\text{f-DTD}}(t)$  shown therein is equivalent to  $\beta_{\text{f-DTD}}(t) = \{\mu_{\text{f-DTD}}(t)\}^{-d/(1+d)}$ .) For those chains,  $\tau_{\text{CLF}}$  and  $\tau_{\text{CR}} = \tau_{\text{CR}}^{[\varepsilon]} = 2\tau_{\text{CR}}^{[G]}$ ; cf. Eqs. 11 and 12 with  $M_1 = M_2 = M$ ) are known, so that the comparison can be straightforwardly made. The results are shown in Figures 19 and 20, where the black arrows indicate the second-moment average viscoelastic relaxation time of the monodisperse chain,  $\langle \tau_{\text{m}}^{[G]} \rangle$  (= product of the zero-shear viscosity and recoverable compliance).

For the linear chains (Figure 19),  $\beta_{\text{f-DTD}}(t)$  (blue circles) agrees with  $\beta_{\text{CR}}(t)$  (red curves) within uncertainties of evaluation of these  $\beta$  ( $\sim$ 10% for each) in the entire range of  $t < \langle \tau_{\text{m}}^{[G]} \rangle$ , namely, during the whole process of viscoelastic relaxation. (For PI 308k at long  $t \sim \langle \tau_{\text{m}}^{[G]} \rangle$ ,  $\beta_{\text{f-DTD}}(t)$  tends to become even smaller than  $\beta_{\text{CR}}(t)$ .) Thus, the CR–Rouse dynamics allows the equilibrated entanglement number  $\beta(t)$  to increase up to  $\beta_{\text{f-DTD}}(t)$  considered in the full-DTD picture. For this

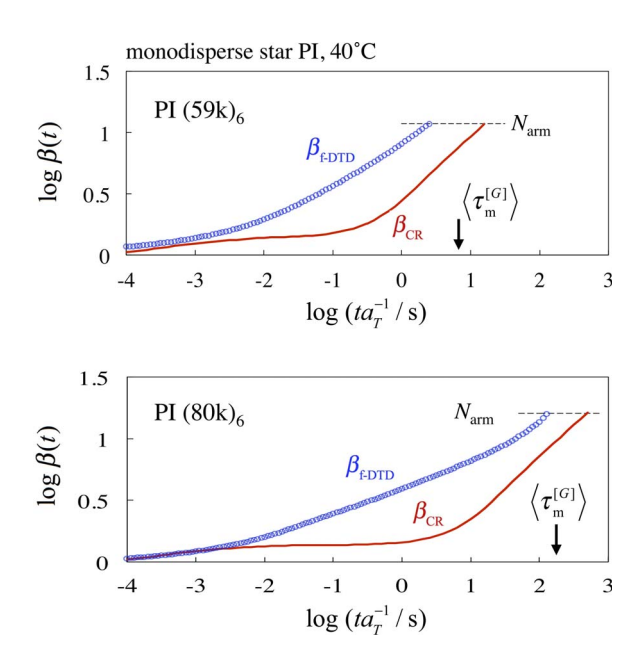


FIG. 20. — Equilibration number of entanglement segments of monodisperse six-arm star PI assumed in the full-DTD molecular picture,  $\beta_{\text{f-DTD}}(t)$  (blue circles). The maximum equilibration number allowed by the CR–Rouse mechanism,  $\beta_{\text{CR}}(t)$ , is shown with red curves. Black horizontal line shows the number of entanglements per star arm,  $N_{\text{arm}}$ .  $\beta_{\text{f-DTD}}(t)$  and  $\beta_{\text{CR}}(t)$  data are taken from Watanabe et al. 36 with permission.

reason, the normalized viscoelastic relaxation function  $\mu_{f\text{-DTD}}(t)$  deduced from this picture agrees with the  $\mu(t)$  data, as noted in Figure 15.

In contrast, for the monodisperse star chains,  $\beta_{\text{F-DTD}}(t)$  is significantly larger than  $\beta_{\text{CR}}(t)$  (by a factor beyond the uncertainty explained above), and thus the CR–Rouse dynamics does not allow the actual  $\beta(t)$  to increase up to  $\beta_{\text{f-DTD}}(t)$  at intermediate to long time scales (at  $t > 10^{-2}$  s); see Figure 20. Consequently,  $\mu_{\text{f-DTD}}(t)$  deviates from the  $\mu(t)$  data at those t, as noted in Figure 16. In fact, in Figure 20, the failure of the full-DTD picture can be noted for  $\beta_{\text{f-DTD}}(t)$  itself:  $\beta_{\text{f-DTD}}(t)$  reaches its maximum possible value,  $\beta_{\text{max}} = N_{\text{arm}}$  (horizontal dashed line) corresponding to the full-DTD picture to work in the terminal relaxation regime. (In contrast, the CR-equilibrated number  $\beta_{\text{CR}}(t)$  remains smaller than  $\beta_{\text{max}}$  in the entire range of  $t < \langle \tau_{\text{m}}^{[G]} \rangle$ .)

Here, it is informative to consider how the full-DTD picture fails for the star chains and works for the linear chains. For an arm of a given (probe) star chain, the fully dilated tube diameter  $a_{\rm f-DTD}'(t)$  (= $a\{\beta_{\rm f-DTD}(t)\}^{1/2}$ = $a\{\phi'(t)\}^{-d/2}$ ) is available as a length scale of equilibration in a time scale of t thanks to the motion of surrounding star chains; however, this length scale is too large for the CR–Rouse motion of the probe arm to explore within that time scale. Such an unusably large  $a_{\rm f-DTD}'(t)$  is a consequence of the broad relaxation mode distribution of the star chains that significantly decreases  $\phi'(t)$  at short t. In contrast, the monodisperse linear chains exhibit a narrow terminal relaxation mode distribution that allows  $\beta_{\rm f-DTD}(t)$  to stay small and comparable to  $\beta_{\rm CR}(t)$  in the entire range of t (cf. Figure 19):  $\beta_{\rm f-DTD}(t) \cong 3 \ll N$  even at  $t = \langle \tau_{\rm m}^{[G]} \rangle$ . This narrow mode distribution, enabling the CR–Rouse motion to cover the length scale of  $a_{\rm f-DTD}'(t)$  in time, is the reason for the validity of the full-DTD picture for the linear chains noted in Figure 15.

For the PI 308k/PI 21k binary blends, we can similarly examine validity of the full-DTD picture. Specifically,  $\beta_{\text{f-DTD}}(t) (= \{\mu_{\text{f-DTD}}(t)\}^{-d/(1+d)} \text{ with } \mu_{\text{f-DTD}}(t) \text{ being shown in Figure 17}) \text{ needs}$ 

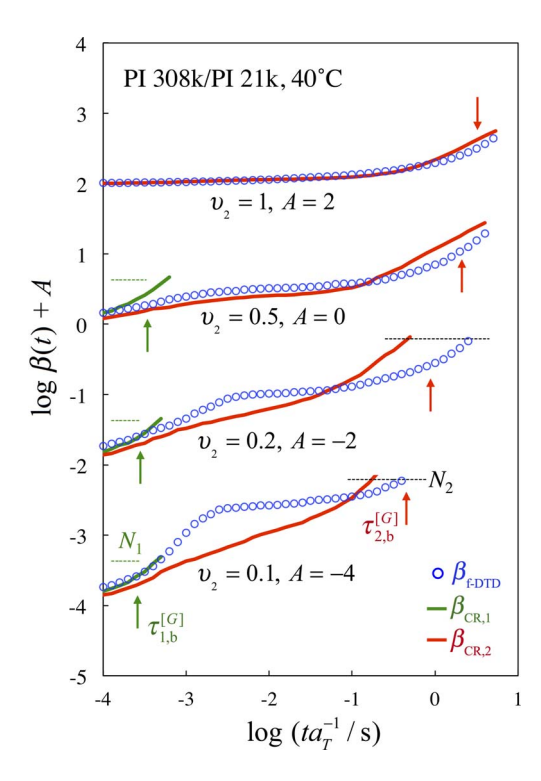


FIG. 21. — Equilibration number of entanglement segments in PI 308k/PI 21k blends assumed in the full-DTD picture,  $\beta_{\rm f}$ . DTD(t) (blue circles). The maximum equilibration numbers for the short and long chains (PI 21k and PI 308k) allowed by the CR–Rouse mechanism,  $\beta_{\rm CR,1}(t)$  and  $\beta_{\rm CR,2}(t)$ , are shown with green and red curves. Horizontal lines show the number of entanglements per short and long chains,  $N_1$  and  $N_2$ . The plots are vertically shifted by the factors A as indicated so as to avoid heavy overlapping. Data are taken from Watanabe et al.  $^{34,35}$  with permission.

to be compared with  $\beta_{CR,1}(t)$  and  $\beta_{CR,2}(t)$  defined for the short and long chains, PI 21k and PI 308k. The comparison is made by separately considering the CR–Rouse times for the long and short chains on the basis of empirical Eq. 11 and by taking into account a dielectrically detected moderate retardation of the short chain relaxation due to the entanglement with the long chains. The results of this comparison are presented in Figure 21. For simplicity,  $\beta_{CR,1}(t)$  and  $\beta_{CR,2}(t)$  used in the comparison were evaluated just for the CR–Rouse relaxation, namely, with the aid of Eq. 20 but without incorporating the CLF contribution. However, for the dominant part of the long chain relaxation at long t, the CLF contribution is minor and the lack of this contribution in  $\beta_{CR,1}(t)$  and  $\beta_{CR,2}(t)$  is not important.

For the blends with a small volume fraction of the long chain,  $v_2$ =0.1 and 0.2, Figure 21 shows that  $\beta_{f\text{-DTD}}(t)$  (blue circle) remains close to  $\beta_{\text{CR},1}(t)$  (green curve) and  $\beta_{\text{CR},2}(t)$  (red curve) at short t up to the terminal relaxation time of the short chain,  $\tau_{1,b}^{[G]}$  (green arrow). (Note also that  $\beta_{\text{CR},1}(t)$  in that range of t remains smaller than its maximum possible value,  $N_1$ , shown with the horizontal green dotted line.) However, at intermediate t where the short chain has fully relaxed and only the long chain sustains the modulus,  $\beta_{f\text{-DTD}}(t)$  becomes considerably larger than  $\beta_{\text{CR},2}(t)$  so that the long chain cannot explore, in time, the length scale of fully dilated tube diameter  $a_{f\text{-DTD}}'(t) = a\{\beta_{f\text{-DTD}}(t)\}^{1/2}$ . Nevertheless, at longer t where  $\beta_{\text{CR},2}(t)$  approaches its maximum possible value,  $N_2$  (horizontal black dotted line),  $\beta_{f\text{-DTD}}(t)$  becomes smaller than  $\beta_{\text{CR},2}(t)$  and the long chain can be

equilibrated over the diameter  $a_{\text{f-DTD}}'(t)$  in time. For those blends, the failure of the full-DTD picture is noted exactly in the intermediate time scale where  $\beta_{\text{f-DTD}}(t) > \beta_{\text{CR},2}(t)$ ; compare Figures 17 and 21 for  $\upsilon_2 = 0.1$  and 0.2. It should be noted that the rapid and intensive relaxation of the short chain leads to a large decrease of  $\varphi'(t)$  and a large increase of  $\beta_{\text{f-DTD}}(t)$  at  $t \geq 2\tau_{1,b}^{[G]}$  (cf. Figure 21) thereby resulting in the failure of the full-DTD picture. This role of the fast relaxation of the short chain in the blends with small  $\upsilon_2$  is similar to that of intensive fast relaxation of the star chains having a broad mode distribution. Consequently, the blend with larger  $\upsilon_2 = 0.5$  exhibits less intensive fast relaxation of the short chain so that its  $\beta_{\text{f-DTD}}(t)$  is only slightly larger than  $\beta_{\text{CR},2}(t)$  at intermediate time scale (cf. Figure 21), which results in just slight failure of the full-DTD picture for this blend (Figure 17). Finally, for  $\upsilon_2 = 1$  (bulk PI 308k),  $\beta_{\text{f-DTD}}(t) \leq \beta_{\text{CR},2}(t)$  and thus the full-DTD picture is valid in the entire range of t up to the terminal relaxation time of the long chain,  $\tau_{2,b}^{[G]}$  (red arrow); cf. Figures 17 and 21.

The results of the test of the full-DTD picture presented in Figures 19–21 clearly indicate that the full-DTD picture fails in the range of t where  $\beta_{f\text{-DTD}}(t) > \beta_{CR}(t)$ . However, the test does not rule out the tube dilation up to  $\beta_{CR}(t)$ . In fact, direct comparison of the viscoelastic and dielectric data of monodisperse PI unequivocally indicates that the entanglement is not fixed in space (cf. Figure 3). Namely, in the terminology of the tube model, the CR/DTD process undoubtedly occurs for the monodisperse polymers. Thus, a molecular picture of partial-DTD is naturally introduced as  $^{24,35,51}$ 

for monodisperse polymers: 
$$\beta_{p-DTD}(t) = min[\beta_{f-DTD}(t), \beta_{CR}(t)]$$
 (23)

The corresponding survival fraction of the partially dilated tube,  $\varphi'(t)$ , is evaluated from the dielectric  $\Phi(t)$  data and the  $\tau_{CR}$  data (=  $\tau_{CR}^{[\epsilon]} = 2\tau_{CR}^{[G]}$ ; cf. Eqs. 11 and 12 with  $M_1 = M_2 = M$ ): the  $\tau_{CR}$  data give  $\beta_{CR}(t) = 1/\psi_{CR}(t)$  through Eqs. 20–22, and Eqs. 15 and 16 combined with Eq. 23 allow us to determine  $\varphi'(t)$  and  $\beta_{p-DTD}(t)$  from the  $\beta_{CR}(t)$  value and the  $\Phi(t)$  data. The viscoelastic  $\mu_{p-DTD}(t)$  for the partial-DTD picture is simply given by Eq. 14 with  $\beta(t) = \beta_{p-DTD}(t)$ . In Figures 15 and 16,  $\mu_{p-DTD}(t)$  thus obtained is shown with the red curves. For monodisperse linear PI,  $\beta_{f-DTD}(t) \leq \beta_{CR}(t)$  (cf. Figure 19) so that  $\mu_{p-DTD}(t)$  coincides with  $\mu_{f-DTD}(t)$  and excellently describes the  $\mu(t)$  data (cf. Figure 15). For monodisperse star PI,  $\mu_{p-DTD}(t)$  is considerably larger than  $\mu_{f-DTD}(t)$  and agrees well with the  $\mu(t)$  data (cf. Figure 16).

For the PI 308k/PI 21k blends, the above partial-DTD picture is extended to separately evaluate  $\beta_{p\text{-DTD}}(t)$  for the short and long chain components (in a way corresponding to that explained for Figure 21), and the resulting  $\mu_{f\text{-DTD}}(t)$  is shown in Figure 17 with the red curve. This  $\mu_{f\text{-DTD}}(t)$  is in excellent agreement with the  $\mu(t)$  data.

All above results indicate that the partial-DTD picture (including the full-DTD picture for the case of  $\beta_{f\text{-DTD}} < \beta_{CR}$ ) is valid for monodisperse PI as well as blends of linear PI. The success of the partial-DTD picture has been confirmed also for Cayley-tree type branched PI. <sup>56</sup> The success of the partial-DTD picture indicates that the tube dilates (i.e., the entanglement loosens) to the maximum length scale allowed by the motion of the tube-forming chains and by the CR motion of the probe chain in a given time scale. In other words, the DTD picture is valid given that the length and time scales are consistently coarse-grained, as noted in Figures 19–21.

It is the comparison of dielectric and viscoelastic data that revealed the success of the partial-DTD picture for describing the entanglement dynamics. This success in turn demonstrates the importance of the comparison of those data. In fact, the comparison is useful also for dipole-inverted PI: coherence of the chain motion in entangled bulk and lack of this coherence in unentangled solutions have been successfully deduced from comparison of the viscoelastic and dielectric data.<sup>28</sup>

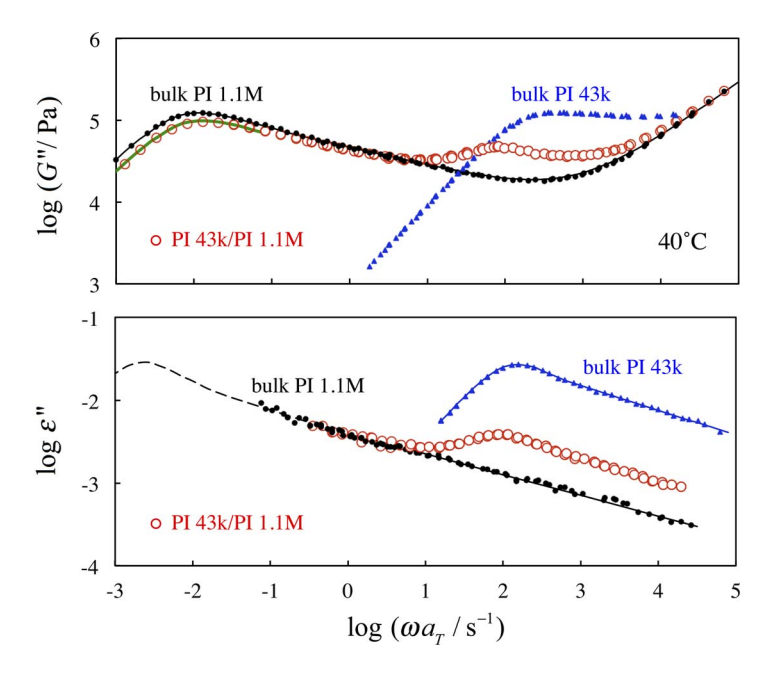


FIG. 22. — Viscoelastic and dielectric data of PI 43k/PI 1.1M blend ( $\upsilon_1$  =0.1) at 40 °C. Data are taken from Matsumiya et al. <sup>37</sup> with permission.

## E. DUALITY OF TUBE FOR RELAXATION TIME AND RELAXATION INTENSITY

For entangled PI having the type-A dipoles, the relationship between the viscoelastic  $\mu(t)$  and dielectric  $\Phi(t)$  data is in accord to the partial-DTD picture that makes consistent coarse-graining of the length and time scales according to the CR–Rouse dynamics, as demonstrated in the analysis shown in Figures 15–17 and 19–21. However, this picture just describes the relationship between the  $\mu(t)$  and  $\Phi(t)$  data (the latter giving  $\varphi'(t)$ ) and does not specify the t dependence of those data. For the terminal relaxation time characterizing this t dependence, the DTD effect has been examined through comparison of the data for PI probe in high-M PI matrix and in monodisperse bulk. <sup>37,40</sup> The results are summarized below.

1. Viscoelastic and Dielectric Data of Linear PI Probe in DTD-Free Environment. — Figure 22 shows viscoelastic and dielectric losses, G'' and  $\epsilon''$ , measured for a PI 43k/PI 1.1M blend containing dilute linear PI 43k probe  $(v_1 = 0.1)$ . The blue triangles and black circles represent the data of PI 43k and PI 1.1M in respective monodisperse bulk. The probe relaxation in the blend is clearly detected as the peak of the G'' and  $\epsilon''$  data at high  $\omega$ ; see red circles. This relaxation is observed also for the G' and  $\{\epsilon_0 - \epsilon'\}$  data, but much less clearly because these data are less sensitive to fast and weak relaxation of the probe compared to the G'' and  $\epsilon''$  data. For this reason, the following discussion focuses on the G'' and  $\epsilon''$  data.

As noted in Figure 22, the probe relaxation is slower in the blend (in the high-M matrix) than in its monodisperse bulk, which suggests that the CR mechanism for the probe is suppressed in the blend. For quantitative discussion of this suppression, the blend data need to be decomposed into the contributions from the probe and matrix (short and long chains). This decomposition can be made on the basis of a general blending rule for the viscoelastic and dielectric loss data of the blend,  $G_b''(\omega)$  and  $\varepsilon_b''(\omega)$ :

$$G_{\mathbf{b}}^{"}(\omega) = v_1 G_{1\,\mathbf{b}}^{"}(\omega) + v_2 G_{2\,\mathbf{b}}^{"}(\omega) \tag{24}$$

$$\varepsilon_{\mathbf{b}}^{"}(\omega) = \upsilon_{1} \varepsilon_{1,\mathbf{b}}^{"}(\omega) + \upsilon_{2} \varepsilon_{2,\mathbf{b}}^{"}(\omega) \tag{25}$$

Here,  $G_{2,b}''(\omega)$  and  $\varepsilon_{2,b}''(\omega)$  represent the viscoelastic and dielectric losses of the long (matrix) chain in the blend reduced by its volume fraction  $\upsilon_2$ , and  $G_{1,b}''(\omega)$  and  $\varepsilon_{1,b}''(\omega)$  are the losses of the short probe reduced by  $\upsilon_1 (= 1 - \upsilon_2)$ .  $G_{2,b}''(\omega)$  and  $\varepsilon_{2,b}''(\omega)$  do not coincide with  $G_{2,m}''(\omega)$  and  $\varepsilon_{2,m}''(\omega)$  of the pure matrix (black circles in Figure 22) because of the partial relaxation of the long matrix chains activated by the short probe motion. However, for the blend with small  $\upsilon_1 (= 0.1 \text{ in Figure 22})$ , we can satisfactorily express  $G_{2,b}''(\omega)$  and  $\varepsilon_{2,m}''(\omega)$  in terms of the  $G_{2,m}''(\omega)$  and  $\varepsilon_{2,m}''(\omega)$  data to evaluate  $G_{1,b}''(\omega)$  and  $\varepsilon_{1,b}''(\omega)$  of the probe of our interest, as explained below.<sup>37</sup>

The top panel of Figure 22 shows that the probe (PI 43k) in the blend has fully relaxed at high  $\omega \cong 10 \, \mathrm{s}^{-1}$ , and the corresponding probe motion activates partial viscoelastic relaxation of the matrix. Consequently, the terminal relaxation of the matrix (and the blend as a whole), seen at much lower  $\omega$ , is faster and less intensive compared to that of the pure matrix. This feature enables us to express  $G_{2,\mathrm{b}''}(\omega)$  of the matrix in the terminal relaxation zone in terms of the  $G_{2,\mathrm{m}''}(\omega)$  data of the pure matrix (black circles in the top panel of Figure 22) as

$$G_{2,\mathrm{b}}^{\text{terminal }''}(\omega) = I_2 G_{2,\mathrm{m}}^{\prime\prime}(\lambda_2^{[G]}\omega) \tag{26}$$

The factors  $I_2$  and  $\lambda_2^{[G]}$  represent the fractional intensity reduction and acceleration of the terminal relaxation of the matrix in the blend. Validity of Eq. 26 is noted in the top panel where the green curve shows the shifted data of pure matrix,  $I_2G_{2,\mathrm{m}}^{''}(\lambda_2^{[G]}\omega)$  with the factors  $I_2=0.89$  and  $\lambda_2^{[G]}=0.89$ . This green curve excellently describes the  $G_b''(\omega)$  data of the blend at low  $\omega$ .

At high  $\omega$  where the probe of our interest (PI 43k) is still relaxing,  $G_{2,b}^{\text{terminal}}(\omega)$  given by Eq. 26 should differ from the actual loss modulus  $G_{2,b}''(\omega)$  of the matrix in the blend, because the matrix entanglement with the probe chains has not fully relaxed at those  $\omega$ . At such high  $\omega$ , the matrix partially relaxes viscoelastically together with the probe. Then, the loss modulus difference of the matrix representing this partial relaxation,  $\Delta G_{2,b}''(\omega) \equiv G_{2,b}''(\omega) - G_{2,b}^{\text{terminal}}(\omega)$ , should be close to  $G_{1,b}''(\omega)$  of the probe in the blend, except that the relaxation intensity is smaller for  $\Delta G_{2,b}''(\omega)$  by a factor of  $1-I_2$  (because the fraction  $I_2$  of the intensity relaxes at low  $\omega$  as represented by  $G_{2,b}^{\text{terminal}}(\omega)$ ). Thus, substituting  $G_{2,b}''(\omega) = \Delta G_{2,b}''(\omega) + G_{2,b}^{\text{terminal}}(\omega) \cong (1-I_2)G_{1,b}''(\omega) + I_2G_{2,m}''(\lambda_2^{[G]}\omega)$  in Eq. 24, we can express  $G_{1,b}''(\omega)$  of the probe in terms of the  $G_b''(\omega)$  and  $G_{2,m}''(\omega)$  data of the blend and pure matrix as

$$G_{1,b}^{"}(\omega) \cong \frac{1}{1 - \nu_2 I_2} \left\{ G_b^{"}(\omega) - \nu_2 I_2 G_{2,m}^{"}(\lambda_2^{[G]}\omega) \right\}$$
 (27)

(Note that a modulus difference corresponding to the above  $\Delta G_{2,b}''(\omega)$  does not appear in Eq. 6 for short matrix chains in the blends examined in Figures 4–6 because those short chains are the major component therein and fully relax within a time scale of the long–short entanglement relaxation.)

The situation is much simpler for dielectric  $\epsilon_{1,b}{}''(\omega)$ . In general, the dielectric relaxation mode distribution (shape of  $\epsilon''$  curve) of linear PI is insensitive to CR/DTD. <sup>23,24,34,35</sup> In the bottom panel of Figure 22, this insensitivity is noted as the similarity of the  $\omega$  dependence of  $\epsilon''$  data of the PI 43k/PI 1.1M blend, bulk PI 43k, and bulk PI 1.1M (matrix) at  $\omega > 300 \, \text{s}^{-1}$ . Thus, the reduced dielectric loss of the matrix appearing in Eq. 25,  $\epsilon_{2,b}{}''(\omega)$ , is satisfactorily expressed in terms of the  $\epsilon_{2,m}{}''(\omega)$  data of the pure matrix as  $\epsilon_{2,b}{}''(\omega) = \epsilon_{2,m}{}''(\lambda_2^{[G]}\omega)$ , where  $\lambda_2^{[G]}$  is the acceleration factor determined for the viscoelastic data. Then, the reduced dielectric loss of the probe PI,  $\epsilon_{1,b}{}''(\omega)$ , is experimentally evaluated as <sup>37</sup> (cf. Eq. 25)

$$\varepsilon_{1,b}^{"}(\omega) = \frac{1}{\upsilon_1} \left\{ \varepsilon_b^{"}(\omega) - \upsilon_2 \varepsilon_{2,m}^{"}(\lambda_2^{[G]}\omega) \right\}$$
 (28)

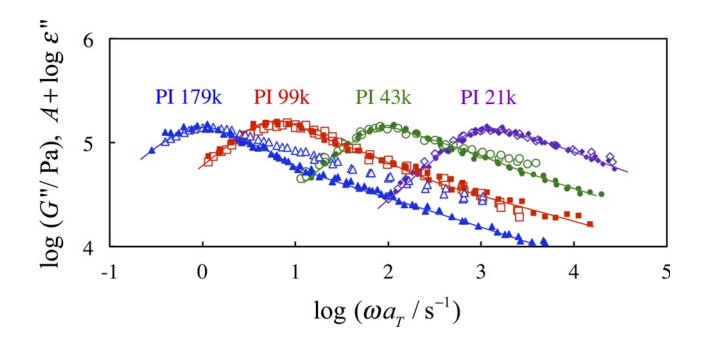


FIG. 23. — Comparison of  $G_{1,b}''$  (unfilled symbols) and  $\varepsilon_{1,b}''$  (filled symbols) of linear PI probe entangled with PI 1.1M matrix at 40 °C. The volume fraction is  $\upsilon_1$  = 0.2 for PI 179k probe and  $\upsilon_1$  = 0.1 for the other three probes. Data are taken from Matsumiya et al.<sup>37</sup> with permission.

Figure 23 compares  $G_{1,b}''(\omega)$  (unfilled symbols) and  $\varepsilon_{1,b}''(\omega)$  (filled symbols) of short probe chains entangled with long matrix (PI 1.1M) thus evaluated from Eqs. 27 and  $28.^{37}$   $\lambda_2^{[G]} = 0.94$  for the PI 179 probe, and  $\lambda_2^{[G]} = 0.89$  for the three other probes. For direct comparison,  $\varepsilon_{1,b}''(\omega)$  is multiplied by a factor of  $10^A$  in order to match its peak height with that of  $G_{1,b}''(\omega)$ , and a contribution from the intrinsic, local Rouse relaxation within the entanglement segment has been subtracted from  $G_{1,b}''(\omega)$ . ( $\varepsilon_{1,b}''(\omega)$  does not have this contribution.) The volume fraction is  $\upsilon_1 = 0.2$  for the PI 179k probe, and  $\upsilon_1 = 0.1$  for the other three probes, PI 21k, PI 43k, and PI 99k. Judging from the effective molecular weight associated to the probe—probe (short—short) entanglement,  $M_{e,pp} = M_{e,bulk PI}/\upsilon_1^{1.3} = 41k$  (for  $\upsilon_1 = 0.2$ ) and  $M_{e,pp} = 100k$  (for  $\upsilon_1 = 0.1$ ), the PI 179k probe chains are mostly entangled with the PI 1.1M matrix but also among themselves moderately, whereas the three shorter probes are entangled only with the matrix.

Here, a comment needs to be added for the probe losses shown in Figure 23. The matrix losses  $G_{2,m}''(\lambda_2^{[G]}\omega)$  and  $\varepsilon_{2,m}''(\lambda_2^{[G]}\omega)$  subtracted in Eqs. 27 and 28 are the extrapolation of the viscoelastic and dielectric losses of the matrix at low  $\omega$  (where the probe has fully relaxed) to high  $\omega$  where the probe is still relaxing. Before completion of the probe relaxation, the matrix would behave more or less similar to that in monodisperse bulk, and its actual losses should be smaller than  $G_{2,m}''(\lambda_2^{[G]}\omega)$  and  $\varepsilon_{2,m}''(\lambda_2^{[G]}\omega)$  appearing in Eqs. 27 and 28. Thus,  $G_{1,b}''(\omega)$  and  $\varepsilon_{1,b}''(\omega)$  shown in Figure 23 should be regarded as the smallest possible viscoelastic and dielectric losses of the probe in the blend. Nevertheless, the largest possible losses obtained from Eqs. 27 and 28 with  $\lambda_2^{[G]} = 1$  were only slightly larger than those shown in Figure 23, as demonstrated in Matsumiya et al. This close coincidence of the smallest and largest possible loss values, reflecting the  $\lambda_2^{[G]}$  value close to unity  $(\lambda_2^{[G]}) \geq 0.89$  for the matrix entangled with the four probes examined in Figure 23), enables us to reliably use  $G_{1,b}''(\omega)$  and  $\varepsilon_{1,b}''(\omega)$  shown in Figure 23 as the real losses of the probes.

For the PI 21k and PI 43k probes,  $G_{1,b}''(\omega)$  agrees surprisingly well with  $10^A \epsilon_{1,b}''(\omega)$  to satisfy Eq. 5b, as clearly noted in Figure 23. This experimental fact indicates that the matrix–probe (long–short) entanglement constraining the probe motion is fixed in space in the time scale of the probe relaxation. Namely, these two probes relax in the DTD-free environment. In fact, the  $\omega$  dependence of their  $G_{1,b}''(\omega)$  and  $\varepsilon_{1,b}''(\omega)$  is very close to that expected for a chain being trapped in a fixed tube and relaxing through reptation and CLF;  $G_{\text{rept+CLF}}'' \sim \varepsilon_{\text{rept+CLF}}'' \sim \omega^{-1/4}$  at high  $\omega$ . For the PI 99k probe, the  $G_{1,b}''(\omega)$  and  $10^A \varepsilon_{1,b}''(\omega)$  data are slightly different around their peaks, which indicates that the DTD mechanism is not perfectly quenched for this probe entangled with the PI 1.1M matrix (because  $M_2$  of the matrix is not sufficiently larger than  $M_1$  of the probe). Finally, for the PI 179k probe having a larger  $M_1$ , a moderate deviation is clearly noted between  $G_{1,b}''(\omega)$  and  $10^A \varepsilon_{1,b}''(\omega)$ , although this deviation is much less prominent compared to the deviation seen for monodisperse

linear PI in bulk; see the top panel of Figure 3 where G'' and  $\varepsilon''$  exhibit significant differences not only in their relaxation mode distribution but also in the peak frequency. This moderate deviation seen for the PI 179k probe emerges because the matrix–probe entanglement relaxes to some extent in the time scale of probe relaxation to activate DTD for the probe (and because the moderate probeprobe entanglement also relaxes to activate DTD).

2. Relaxation Time in DTD-Free Environment. — In relation to the validity of the DTD picture discussed for Figures 15–17, it is informative to examine the magnitude of acceleration of the relaxation due to DTD. For monodisperse linear PI chains, the full-DTD relationship (Eqs. 14 and 17) is valid between the viscoelastic  $\mu(t)$  and the dielectrically evaluated tube survival fraction  $\varphi'(t)$ , as revealed in Figure 15. This validity reflects the narrow relaxation mode distribution of the linear chains that allows the number  $\beta(t)$  of the equilibrated entanglement segments to stay small; in Figure 19,  $\beta(t)$  associated to the terminal viscoelastic relaxation is evaluated as  $\beta_{\mu} \cong 3$  (log  $\beta_{\mu} \cong 0.5$ ) at  $t = \langle \tau_m^{[G]} \rangle$  for all linear PI samples examined.

If the relaxed portion of the chain behaves as a solvent in all aspects of the relaxation dynamics of monodisperse linear PI chains (i.e., not only for the relationship between  $\mu(t)$  and  $\phi'(t)$ ), then the terminal relaxation time of the monodisperse linear PI chain,  $\tau \sim M^{3.5}/M_e^{1.5}$ , is naively expected to increase by a factor of  $\beta_{\mu}^{1.5} \cong 5$  when the CR/DTD mechanism working in the monodisperse bulk system is quenched. (The effective entanglement molecular weight determining the relaxation time should be proportional to  $\beta_{\mu}$  if the relaxed portion behaves as the solvent in all aspects.) In the following, this expectation is tested with the aid of the data shown in Figure 23.

For the PI probes examined in Figure 23, we can evaluate the viscoelastic and dielectric relaxation times,  $\tau_{1,b}^{[G]}$  and  $\tau_{1,b}^{[\epsilon]}$ , as reciprocal of the peak frequencies of the  $G_{1,b}''(\omega)$  and  $\varepsilon_{1,b}''(\omega)$  data. (The corresponding "storage parts" of those probes,  $G_{1,b}'(\omega)$  and  $\varepsilon_{1,b}'(\omega)$ , cannot be accurately evaluated because  $G_b'(\omega)$  and  $\Delta\varepsilon_b'(\omega)$  data of the blends are rather insensitive to the fast and weak relaxation of the probes having small  $\upsilon_1$  (=0.1 or 0.2). For this reason, the second-moment average relaxation time (cf. Eq. 7) cannot be used in the discussion below.) From the  $G_{1,m}''(\omega)$  and  $\varepsilon_{1,m}''(\omega)$  data of the probes in the monodisperse bulk state, the relaxation times  $\tau_{1,m}^{[G]}$  and  $\tau_{1,m}^{[\varepsilon]}$  are similarly evaluated as reciprocal of the peak frequencies. The relaxation mode distribution of  $\varepsilon_{1,b}''(\omega)$  in the blends agrees with that of the  $\varepsilon_{1,m}''(\omega)$  data of monodisperse bulk PI,  $\varepsilon_{1,m}^{[\varepsilon]}$  so that the  $\varepsilon_{1,b}^{[\varepsilon]}/\tau_{1,m}^{[\varepsilon]}$  ratio is equivalent to a ratio of the *longest* dielectric relaxation times in the fixed and unfixed entanglement environments. This is not the case for the viscoelastic data: the mode distribution is narrower for  $G_{1,b}''(\omega)$  than for  $G_{1,m}''(\omega)$  (cf. Figures 22 and 23), and thus the  $\varepsilon_{1,b}^{[G]}/\tau_{1,m}^{[G]}$  ratio should be somewhat different from (larger than) the ratio of the longest viscoelastic relaxation times. However, this small difference does not affect the following discussion that mainly focuses on the dielectric  $\varepsilon_{1,b}^{[\varepsilon]}/\tau_{1,m}^{[\varepsilon]}$  ratio.

mainly focuses on the dielectric  $\tau_{1,b}^{[\epsilon]}/\tau_{1,m}^{[\epsilon]}$  ratio.

For the four PI probes examined in Figure 23, Figure 24 shows plots of the  $\tau_{1,b}^{[\epsilon]}/\tau_{1,m}^{[\epsilon]}$  and  $\tau_{1,b}^{[G]}/\tau_{1,m}^{[G]}$  ratios evaluated above<sup>37</sup> against the entanglement number per probe chain,  $M_1/M_e$  (=4.2–35.8); see green circles. For comparison, black squares show the ratios obtained for shorter, lightly entangled probes in their bulk and in the PI 1.1M matrix (after minor correction of the monomeric friction in bulk). The red curves are the results of CR–Rouse analysis explained later. The high-M matrix should have no effect on the relaxation time of *unentangled* probe if the monomeric friction is kept constant, whereas the matrix effect (suppression of CR/DTD) should become prominent for the entangled probe. This behavior is clearly noted in Figure 24 on the increase of  $M_1/M_e$  from 1 to  $\sim$ 4. A further increase of  $M_1/M_e$  results in gradual decreases of the  $\tau_{1,b}^{[\epsilon]}/\tau_{1,m}^{[\epsilon]}$  and  $\tau_{1,b}^{[G]}/\tau_{1,m}^{[G]}$  ratios, and thus the matrix effect becomes less prominent with increasing  $M_1/M_e$ ; see four green circles.

thus the matrix effect becomes less prominent with increasing  $M_1/M_c$ ; see four green circles. In the entire range of  $M_1/M_c$ , the dielectric  $\tau_{1,b}^{[\epsilon]}/\tau_{1,m}^{[\epsilon]}$  ratio (top panel of Figure 24) is significantly smaller than the naively expected ratio explained above,  $\tau_{1,b}^{[\epsilon]}/\tau_{1,m}^{[\epsilon]} \cong \beta_{\mu}^{1.5} \cong 5$  (log  $\tau_{1,b}^{[\epsilon]}/\tau_{1,m}^{[\epsilon]} \cong 0.7$ ). This experimental fact indicates that the relaxed portion of the chains *does not* behave as a solvent with respect to the end-to-end relaxation time of the probe, despite the fact that

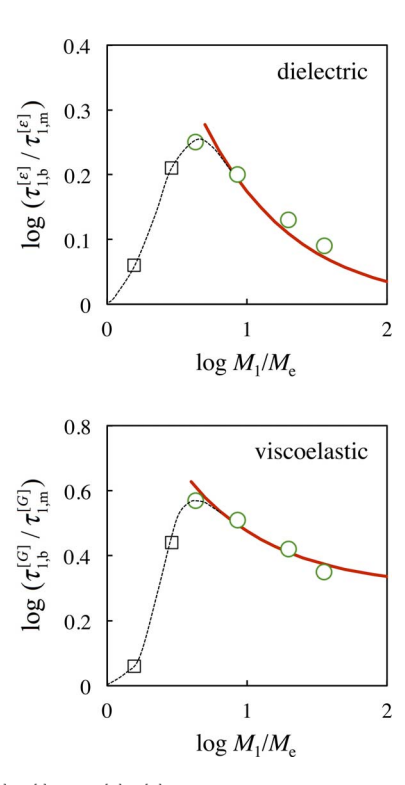


FIG. 24. — Relaxation time ratios  $\tau_{1,b}^{[\epsilon]}/\tau_{1,m}^{[\epsilon]}$  and  $\tau_{1,b}^{[G]}/\tau_{1,m}^{[G]}$  experimentally evaluated for PI probes in the blends with PI 1.1 M matrix and in monodisperse bulk at 40 °C. Red curves show the results of CR–Rouse analysis. Note that the full scale of the vertical axis in the bottom panel is twice of that in the top panel. Data are taken from Watanabe et al.  $^{37,39}$  with permission.

the viscoelastic  $\mu(t)$  data and the dielectrically evaluated  $\phi'(t)$  of monodisperse linear PI obey the full-DTD relationship (cf. Figure 15). This relationship is just based on the molecular picture that the relaxed portion of the chains, having the fraction  $1-\phi'(t)$ , widens the entanglement mesh (modeled as the tube) to the level in a solution having a concentration  $\phi'(t)$ . Namely, the full-DTD relationship does not specify anything related to the chain motion in the dilated tube over a length scale greater than dilated tube diameter. In contrast, the naive expectation is based on an assumption that the chain moves *along* the dilated tube with its intrinsic friction. Thus, the deviation between the  $\tau_{1,b}^{[\epsilon]}/\tau_{1,m}^{[\epsilon]}$  data and the expectation is not contradictory to the validity of the full-DTD relationship between  $\mu(t)$  and  $\phi'(t)$  but suggests a hypothesis explained below.

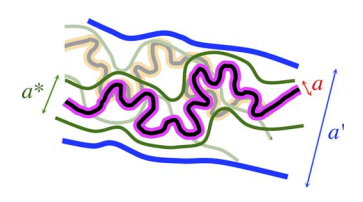


FIG. 25. — Illustration of dual tube for a linear chain in monodisperse bulk. The a is the diameter of undilated tube, and a' is the diameter of fully dilated tube that specifies the range of lateral motion of the chain to describe the extra modulus decay due to DTD. A tube specifying the longitudinal motional path of the chain has the diameter  $a^*$  (< a') and wriggles in the dilated tube.

From the above deviation, the linear PI chain in the monodisperse bulk appears to be longitudinally moving *not* along the fully dilated tube but along a thinner tube that wriggles in the fully dilated tube, as illustrated in Figure 25. The dilated tube, being introduced as a model to represent the loosening of the entanglement constraint, seems to have a dual structure.<sup>37</sup> A wide tube having the diameter a' describes the constraint for the chain motion in a direction *lateral* to the chain backbone, thereby describing the extra decay of the viscoelastic modulus on the entanglement loosening (by the full-DTD factor of  $\{a/a'\}^2 = \{\phi'\}^d$  for monodisperse linear chains). In contrast, a thinner tube having the diameter  $a^*$  (with  $a < a^* < a'$ ) specifies the *longitudinal* motional path of the chain that determines the dielectric relaxation time  $\tau_{1,m}^{[\varepsilon]}$  (=end-to-end fluctuation time), and the wriggling motion of this path tube in the wider tube allows the lateral equilibration over the length scale of a' and the corresponding modulus decay to occur. Within this hypothesis, the viscoelastic relaxation time  $\tau_{1,m}^{[G]}$  is affected by this modulus decay on the entanglement loosening, and thus the suppression of the loosening (i.e., blending in the high-M matrix) increases the viscoelastic  $\tau_1^{[G]}$  of the probe more significantly than the dielectric  $\tau_1^{[\varepsilon]}$ , which is consistent with the observation in Figure 24. In the following, the dual tube hypothesis is tested through a simple CR–Rouse analysis.

3. CR-Rouse Analysis of Relaxation Time. The best already at the state analysis of Relaxation Time (end-to-end fluctuation time)  $\tau_{1,m}^{[\epsilon]}$  of the linear PI chain in its monodisperse bulk. This  $\tau_{1,m}^{[\epsilon]}$  is assigned as the time required for reptation (after CLF) along the motional path tube having the diameter  $a^*$  (cf. Figure 25). For this reptation to occur, all dilated segments of the size  $a^*$  should balance their tension through simultaneous CR-equilibration because of the coherent nature of the reptative motion. This simultaneous CR-equilibration occurs through accumulation of local CR-equilibration in all dilated segments.

The number of those dilated segments per chain is given by  $N^* = N/\beta^*$ , where  $\beta^* = (a^*/a)^2$  is the number of entanglement segments per dilated segment. Among N entanglement segments of the chain,  $N^*$  segments (one for each dilated segment) remain as independent segments specifying the spatial position of the dilated segments, so that the number of entanglement segments to be involved in the simultaneous CR-equilibration is given by

$$g = N - N/\beta^* + 1 \tag{29}$$

Here, the extra factor of "1" has been introduced to satisfy two extreme conditions, g=N for  $\beta^*=N$  (for CR-equilibration of all entanglement segments) and g=1 for  $\beta^*=1$  (for the case of no dilation). The extra factor is necessary to satisfy those conditions but hardly affects the result of the following analysis because the analysis gives  $g \gg 1$  for large N.

For the reptation (after CLF) along the longitudinal motional path tube of the diameter  $a^*$  to occur in time, the characteristic time for the simultaneous CR-equilibration of g entanglement segments,  $\tau_{\text{sim-CR}}$ , should not exceed the longest dielectric relaxation time  $\tau_{1,\text{m}}^{[\epsilon]}$  corresponding to this reptation. This  $\tau_{\text{sim-CR}}$  is dependent on g and thus on  $\beta^* (= \{a^*/a\}^2)$ ; cf. Eq. 29. Because the tube would be dilated to the maximum possible diameter,  $\beta^*$  for a linear PI chain in the monodisperse bulk can be determined from a condition,

$$\tau_{\text{sim-CR}} = \tau_{1.m}^{[\epsilon]} \tag{30}$$

The simultaneous CR-equilibration of g entanglement segments in the monodisperse bulk corresponds to  $p^*$ -th CR-Rouse mode therein, with the mode index  $p^*$  being specified as<sup>37</sup>

$$\frac{1}{p^*} = \frac{(N-2)g+1}{(N-1)^2} \left( \to \frac{g}{N} \text{ for } N \gg 1 \right)$$
 (31)

For  $N \gg 1$ ,  $p^*$  is given by N/g as simply expected from the number of entanglement segments involved between nodes of sinusoidal CR-Rouse eigenfunction. From consideration of two

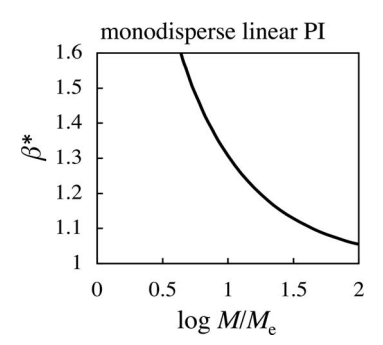


FIG. 26. — Number  $\beta^*$  of the entanglement segments per dilated segment of the size  $a^*$  at the longest dielectric relaxation time  $\tau_{1,m}^{[\epsilon]}$  experimentally evaluated through CR–Rouse analysis for monodisperse linear PI at 40 °C. Data are taken from Matsumiya et al. <sup>37</sup> with permission. For further detail, see text.

extreme conditions,  $p^*=1$  for g=N and  $p^*=N-1$  (the highest CR–Rouse mode index) for g=1, the main expression in Eq. 31 is obtained as a minor correction of the case of  $N \gg 1$ .<sup>37</sup> Using  $p^*$  thus specified as a function of g and N,  $\tau_{\text{sim-CR}}$  is expressed in the CR–Rouse form as

$$\tau_{\text{sim-CR}} = \tau_{\text{CR,m}}^{[\varepsilon]} \sin^2\left(\frac{\pi}{2N}\right) \sin^{-2}\left(\frac{p^*\pi}{2N}\right) \left( \to \frac{\tau_{\text{CR,m}}^{[\varepsilon]}}{p^{*2}} \text{ if } p^* \ll N \right)$$
(32)

Here,  $\tau_{\text{CR,m}}^{[\epsilon]}$  (= $2\tau_{\text{CR,m}}^{[G]}$ ) is the longest dielectric CR time for the monodisperse bulk PI specified experimentally by Eq. 11 with  $M_1 = M_2 = M$ . From Eqs. 30 and 32 together with the data of  $\tau_{1,\text{m}}^{[\epsilon]}$  (= $4.2 \times 10^{-19} M^{3.5}$  s; determined from the  $\epsilon''$  peak frequency for entangled monodisperse linear PI at 40 °C<sup>37</sup>), we can evaluate the CR mode index  $p^*$  and further convert this  $p^*$  into the number of entanglement segments involved in the simultaneous CR-equilibration, g (cf. Eq. 31).

The number  $\beta^*$  of the entanglement segments per dilated segment of the size  $a^*$  at  $t=\tau_{1,m}^{[\epsilon]}$  is directly obtained from the g value thus determined (cf. Eq. 29). Figure 26 shows changes of  $\beta^*$  with the entanglement number  $M/M_e$  (= N) of monodisperse linear PI in bulk.  $\beta^*$  gradually decreases with increasing  $M/M_e$  but does not reach its asymptote ( $\beta^*=1$ ) even at  $M/M_e=100$ . This result suggests that the dielectric relaxation time  $\tau_{1,m}^{[\epsilon]}$  is still affected by the CR/DTD mechanism even in such a well-entangled state (which gives a proof against CR/DTD-independence of  $\tau_{1,m}^{[\epsilon]}$  argued in the literature<sup>22</sup>). More importantly,  $\beta^*$  defined for the longitudinal motional path of the chain is well below the number  $\beta_{\mu} \cong 3$  of the laterally equilibrated entanglement segments. This difference between  $\beta^*$  and  $\beta_{\mu}$  lends support to the hypothesis of the dual structure of the tube illustrated in Figure 25:  $a^* = a \ \beta^{*1/2} < a' = a \beta_{\mu}^{1/2}$  in the time scale of terminal relaxation so that the tube specifying the longitudinal motional path of the chain wriggles laterally in the wider tube (with the diameter a'), the latter describing the extra decay of viscoelastic  $\mu(t)$  due to DTD.

Now we examine the dielectric  $\tau_{1,b}^{[\epsilon]}/\tau_{1,m}^{[\epsilon]}$  ratio of linear PI probe in the high-M matrix (PI 1.1M) and in the monodisperse bulk. Because the local friction of the entanglement segment,  $\zeta_e$ , is the same in these two environments, this ratio is simply given by

$$\frac{\tau_{1,b}^{[\epsilon]}}{\tau_{1,m}^{[\epsilon]}} = \beta^{*1.5} \tag{33}$$

(Note that  $\tau_1^{[\epsilon]} \propto \zeta_e M^{3.5}/M_{e,eff}^{1.5}$  and  $\beta^*$  is equivalent to the ratio of the effective entanglement molecular weight for the chain motion,  $M_{e,eff}$ , in the monodisperse bulk and in the high-M matrix.) The  $\tau_{1,m}^{[\epsilon]}/\tau_{1,m}^{[\epsilon]}$  ratio thus evaluated from  $\beta^*$  (Figure 26) is shown in the top panel of Figure 24 with the

red curve. This curve excellently describes the  $\tau_{1,b}^{[\epsilon]}/\tau_{1,m}^{[\epsilon]}$  data for the moderately- to well-entangled PI probes (green circles).

Furthermore, the viscoelastic relaxation time ratio is simply evaluated as  $\tau_{1,b}^{[G]}/\tau_{1,m}^{[G]}=2\beta^{*1.5}$ , because  $\tau_{1,b}^{[G]}=\tau_{1,b}^{[\epsilon]}$  in the DTD-free high-M matrix (as noted from the agreement of the  $G_{1\cdot b}$ " and  $\varepsilon_{1\cdot b}$ " data for short probes; cf. Figure 23) whereas  $\tau_{1,b}^{[G]}=\tau_{1,m}^{[\epsilon]}/2$  in monodisperse bulk as confirmed experimentally.  $^{24,30,34,35,37}$  The viscoelastic  $\tau_{1,b}^{[G]}/\tau_{1,m}^{[G]}$  ratio thus deduced, shown with the red curve in the bottom panel of Figure 24, is surprisingly close to the data (green circles).

The above success of the simple CR–Rouse analysis for the  $\tau_{1,b}^{[\epsilon]}/\tau_{1,m}^{[\epsilon]}$  and  $\tau_{1,b}^{[G]}/\tau_{1,m}^{[G]}$  ratios, noted also for star PI<sup>40</sup> (for which the motional path tube is wriggling in a partially dilated tube describing the  $\mu(t)$  data in Figure 16), lends support to the hypothesis of the dual tube structure. It should be noted that the CR–Rouse analysis for the linear PI chain just considers the consistent coarse-graining of the length and time scales together with the coherent nature of the reptative motion. From that success, we expect that the dielectric  $\tau_{1,b}^{[\epsilon]}/\tau_{1,m}^{[\epsilon]}$  ratio approaches unity, whereas the viscoelastic  $\tau_{1,b}^{[G]}/\tau_{1,m}^{[G]}$  ratio (=  $2\tau_{1,b}^{[\epsilon]}/\tau_{1,m}^{[\epsilon]}$ ) approaches 2 for the linear PI chain in the high-M limit (although this limit is not covered by experiments). This behavior of the viscoelastic  $\tau_{1,b}^{[G]}/\tau_{1,m}^{[G]}$  ratio corresponds to the Viovy–Rubinstein–Colby<sup>62</sup> (VRC) scenario considering reptation along the *undilated* tube that laterally wriggles in the dilated tube. We also note a consequence of this VRC scenario for highly entangled blends of linear chains: we expect that the terminal viscoelastic relaxation of concentrated long chains therein is not accelerated by the short chains but the decrease of its intensity (decrease of the long–long entanglement plateau modulus at low  $\omega$ ) scales as  $\upsilon_2^{1+d}$  with  $d \cong 1.3$ , whereas the terminal viscoelastic relaxation of the short chain is retarded by the long chains (by a factor of 2 if the short chain is dilute). Indeed, this expectation is in accord with the  $G^*$  data of highly entangled polybutadiene blends reported by Struglinski and Graessley (see figure 9 of Struglinski and Graessley<sup>63</sup>).

#### F. COMMENTS ON RECENT THEORETICAL MODEL/ANALYSIS

This article adopts an experimental viewpoint as much as possible to review the results of analysis of the viscoelastic and dielectric data reflecting the CR/DTD process. Nevertheless, it is also informative to add brief comments for recent theoretical model/analysis of the CR/DTD process<sup>60,61,64,65</sup> and for a feature of the interchain constraints (observed as the entanglement) <sup>66–70</sup> that can be related to the tube dilation exponent. Those comments are summarized below.

1. Tube Dilation Exponent and Feature of Interchain Constraint. — The value of the tube dilation exponent d has been a long-standing subject of theoretical discussion. <sup>60,61</sup> Van Ruymbeke and coworkers <sup>60</sup> focused on blends of long and short linear chains to conclude, from a theoretical argument for the binary nature of entanglement (resulting from the pair-wise constraint between the chains), that d should be 1 just after the relaxation of entanglement of the long chain with the short chain. They also considered that the CR-activated tension re-equilibration <sup>26</sup> follows this long—short entanglement relaxation to effectively increase d up to  $4/3 \cong 1.3$ ). <sup>60</sup> Their model, deduced from this consideration, well describes the viscoelastic data of the PI 308k/PI 21k blends (cf. Figure 14 of this article) by using the dielectric data as the reference. <sup>60</sup> Later, they refined their model based on the time marching algorithm, and this refined model describes both dielectric and viscoelastic data of the PI 308k/PI 21k blends simultaneously (i.e., without using the reference data) as well as viscoelastic data of other blends. <sup>64</sup>

Larson and coworkers<sup>61</sup> examined the terminal viscoelastic relaxation time of "solutions" of high-M monodisperse star polybutadienes (PB) in much shorter, unentangled PB. They focused on very strong dependence of this relaxation time on an effective number of entanglements per star arm,  $N_{\text{arm}} = v_2^d M_{\text{arm}} / M_{\text{e-bulk}}$  with  $v_2$  being the volume fraction of the star, and concluded that the relaxation time is more universally dependent on  $N_{\text{arm}}$  calculated with d=1 than on  $N_{\text{arm}}$  with d=4/

3. This conclusion suggests that the *terminal* relaxation of star PB solutions is better described with d=1 rather than with d=4/3, although a considerable scatter (by a factor of  $\sim 10$ ) is noted for the relaxation times for different sets of  $M_{\rm arm}$  and  $v_2$  giving the same value of  $N_{\rm arm}$  for d=1; see figures 9–12 of Larson et al.<sup>61</sup> (where several different values of  $M_{\rm arm}$  were examined for each star PB sample).

We note an important difference in the d values explained above: for the entangled blends of linear PI chains, van Ruymbeke and coworkers  $^{60,64}$  deduced an increase of the effective d from 1 to 4/3 with increasing t, namely, the effective d value of 4/3 in the terminal relaxation regime. In contrast, for the entangled star PB solutions, Larson and coworkers  $^{61}$  deduced d=1 in the terminal regime. This difference might reflect dual (dynamic and static) aspects of the dilation exponent, as discussed by Larson and coworkers.  $^{61}$  At the same time, one might also suspect that the d value changes with either the chemical structure or the topological architecture (or both) of polymers. The data for highly entangled blends of linear PB (chemically identical to the star PB examined by Larson and coworkers  $^{61}$ ) unequivocally suggest  $d \cong 1.3$  in the terminal regime; see the data for 41L/435L blends in figures 9 and 12 of Struglinski and Graessley.  $^{63}$  Thus, the d value might change with the topological architecture of the chain, or more specifically, with the basic mechanism of relaxation (reptation or arm retraction) determined by this architecture, as judged from the difference of the d values for the linear PI blends and the star PB solutions. A further study is desired for this problem.

Now, we turn our attention to a correlation between the d value deduced by van Ruymbeke and coworkers,  $^{60,64}d=1$  and 4/3 at short and long t, and the d value (= 1.3) incorporated in the partial-DTD picture explained in this article. These two sets of the d values are not necessarily contradicting to each other, because the partial-DTD modulus  $\mu_{p\text{-DTD}}(t)$  in this picture is affected by the d value only in a range of t where  $\beta_{f\text{-DTD}}(t) = \{\phi'(t)\}^{-d} \le \beta_{CR}(t)$  (cf. Eq. 23). This point can be further examined for PI blends with small  $\nu_2$ , for example, the PI 308k/PI 21k blend with  $\nu_2$ =0.1 examined in Figures 17 and 21. In a wide range of t where the short PI 21k chains in the blend have fully relaxed but the long PI 308k chains still exhibit a plateau of  $\mu(t)$  due to the entanglement among themselves,  $\beta_{f\text{-DTD}}(t)$  exceeds  $\beta_{CR,2}(t)$  of the long chain (cf. Figure 21) so that the partial-DTD modulus  $\mu_{p\text{-DTD}}(t)$ , well mimicking the  $\mu(t)$  data, is significantly larger than the full-DTD modulus  $\mu_{f\text{-DTD}}(t)$  (cf. Figure 17). In that range of t,  $\mu_{p\text{-DTD}}(t)$  is contributed only from the long chain and expressed as  $^{35}$   $\mu_{p\text{-DTD}}(t) = \phi'(t)/\beta_{CR,2}(t)$ . This expression does not include the dilation exponent, but we can still define an apparent exponent  $d_{app}$  for  $\mu_{p\text{-DTD}}(t)$  and  $\beta_{CR,2}(t)$  as

$$\mu_{p-DTD}(t) = \{\phi'(t)\}^{1+d_{app}}, \ \beta_{CR,2}(t) = \{\phi'(t)\}^{-d_{app}}$$
(34)

This  $d_{\rm app}$  changes with t, and  $\mu_{\rm p-DTD}(t)$  and  $\beta_{\rm CR,2}(t)$  of the PI 308k/PI 21k blend with  $\upsilon_2$ =0.1 (shown in Figures 17 and 21) give  $d_{\rm app}$  = 0.98 and 1.3 at t =  $10^{-2}$  and  $10^{-1}$  s, respectively. Namely, the partial-DTD picture for the PI blend gives  $d_{\rm app}$  that increases from  $\approxeq 1$  to 1.3 with time (after the relaxation of the short chain component), which is essentially the same as the evolution of d considered in the model by van Ruymbeke and coworkers. Nevertheless, it should be emphasized that  $d_{\rm app}$  is just an apparent dilation exponent, and the partial-DTD picture does not give the power-law relationship, Eq. 34, in the range of t where  $\beta_{\rm f-DTD}(t) > \beta_{\rm CR,2}(t)$ .

Concerning this point, we would like to add that the experimentally observed difference of the CR relaxation behavior of chemically different PI and PS probes (Figures 11 and 12) well fits in the partial-DTD picture through the chemistry-dependent number z of local constraints per entanglement considered in Graessley's CR–Rouse model. <sup>42</sup> It is not clear if this difference of the CR behavior due only to the chemical difference is straightforwardly deduced within the CR–Rouse model *given that* the entanglement exclusively results from the binary (pair-wise) constraint corresponding to d=1.

For this problem, it would be informative to briefly visit the results of molecular dynamics (MD) simulations. Everaers and coworkers<sup>66</sup> made the primitive path analysis based on the MD simulation to visualize interchain hooking (or nodes) attributable to the binary entanglement and demonstrated good agreements between the plateau modulus deduced from this analysis and the literature data. Such nodes, *defined in a static (and statistical) sense*, are observed also in simulations with different algorithms, for example, the "contour reduction topological analysis" by Tzoumanekas and Theodorou<sup>67</sup> and the "direct topological analysis" by Kröger and coworkers.<sup>68</sup> At the same time, the simulation by Likhtman and Ponmurugan<sup>69</sup> revealed that (coarse-grained) chains form mutual contacts in a dynamic sense at many places along their backbone, and these contacts are tight and long-lived. Likhtman<sup>70</sup> further showed that those contacts involve *both* binary and ternary entanglements.

Summarizing these simulation results, one may arrive at a hypothetical molecular view that the interchain constraint has static and dynamic aspects, and both binary and multiple-chain constraints can be dynamically observed as the entanglement: probabilities of forming respective constraints may change according to the chemical structure and topological architecture of the chain. Within the context of the tube model incorporating the CR/DTD mechanism, this molecular view could lead to the (effective) dilation exponent d > 1 in the terminal relaxation regime where both binary and multiple-chain constraints loosen to dynamically dilate the tube. This possible scenario of d is an interesting subject of research, but a further discussion of it goes well beyond the scope of this article emphasizing an experimental viewpoint for analysis of the viscoelastic and dielectric data. A rigid theoretical study is desired for the behavior of d (and for the underlying molecular view).

2. Duality in Description of Reptation along Tube. — In relation to the reptation along the motional path tube (cf. Figure 25), a comment needs to be made for the local friction of the entanglement segment,  $\zeta_e$ . In the CR–Rouse analysis (Eqs. 29–33),  $\zeta_e$  is treated as the intrinsic friction being identical in the high-M matrix (CR/DTD-free environment) and in the monodisperse bulk. This treatment is consistent with the definition of the friction for the chain motion along the motional path tube having the diameter  $a^*$ . However, as an equivalent treatment, we may also introduce an effective friction  $\zeta_{e,eff}$  for the chain motion along the partially/fully dilated tube having the diameter a' ( $>a^*$ ). This dilated tube specifies the range of lateral equilibration of the entanglement segments corresponding to the DTD relaxation of viscoelastic  $\mu(t)$ , and the motion along the dilated tube requires a waiting time  $t_w$  for an extra tension equilibration along it. This waiting time can be cast as an increase of  $\zeta_{e,eff}$  ( $>\zeta_e$ ). Thus, there is a duality in description of the chain motion, for example, reptation along the motional path tube with the diameter  $a^*$  (cf. Figure 25) occurring with the intrinsic  $\zeta_e$ , or, reptation along the dilated tube with the diameter a' occurring with  $\zeta_{e,eff}$ . These two types of reptative motion should give the same  $\mu(t)$  at  $t > t_w$  and the same terminal relaxation time.

In fact, an analysis of the waiting time  $t_{\rm w}$  in blends of linear PI well describes the relaxation time of the long and short chains therein<sup>38</sup> (to an extent similar to that seen in Figure 24). More quantitatively, van Ruymbeke and coworkers<sup>64</sup> analyzed  $t_{\rm w}$  in their model to excellently describe not only the relaxation time but also the frequency dependence of the  $G^*$  and  $\epsilon''$  data of those linear PI blends. They further extended their model to entangled blends of star and linear chains (while keeping the analysis of  $t_{\rm w}$ ) to describe the  $G^*$  data of the blends.<sup>65</sup> Read and coworkers<sup>54</sup> made detailed analysis of  $\zeta_{\rm e,eff}$  (equivalent to  $t_{\rm w}$ ) to specify several different regimes to be added in the Viovy–Rubinstein–Colby (VRC) diagram<sup>62</sup> and compared their results with experimental data and simulation results. Their analysis needed a hypothetical reference state where the intrinsic  $\zeta_{\rm e}$  governs the reptation along the tube; this reference state cannot be the monodisperse bulk wherein the CR/DTD mechanism is already operating. Except this point, their analysis allows us to test differences in the modes of relaxation in the VRC diagram in a purely experimental way.

The above duality in description of chain motion along the dilated tube is a natural consequence of coarse-graining. That is, if we average the chain conformation over every  $t_w$ , the chain would look like a fuzzy thread with the lateral width of a', and its motion would look like 1D motion along the dilated tube. Furthermore, the bead-spring (Rouse) model underlying the tube model gives the same terminal relaxation behavior irrespective of the choice of the bead size as long as the chain is composed of many beads, which is regarded as the duality in the simplest form. Such a duality in description of the chain motion is important in polymer physics and deserves further attention.

#### III. CONCLUDING REMARKS

This review article adopts an experimental viewpoint as much as possible to summarize results of analysis of linear viscoelastic and dielectric data (mostly for PI) and discusses some detailed aspects of the entanglement-loosening mechanism resolved from the analysis. This loosening mechanism, known as the constraint release (CR) and dynamic tube dilation (DTD) mechanisms in the tube model, is unequivocally operating in the monodisperse bulk systems of linear and star PI chains, as revealed from simple comparison of their viscoelastic and dielectric data.

Based on this experimental confirmation of the CR/DTD mechanisms, the survival fraction of the dilated tube  $\varphi'(t)$  is obtained from analysis of the dielectric data, and comparison of  $\varphi'(t)$  and the viscoelastic data indicates validity of the molecular picture of partial-DTD. In this molecular picture, the tube for a given probe chain dilates up to the maximum level allowed by motion of the tube-forming chains and by the CR–Rouse motion of the probe itself. If the probe motion occurs *in time* over the maximum length scale allowed by the motion of the tube-forming chains, the partial-DTD picture reduces to the full-DTD picture wherein the relaxed portion of the chains behaves as a solvent. In this way, the partial-DTD picture makes consistent coarse-graining of the time and length scales, and the diameter of the partially dilated tube represents a spatial length scale of CR-equilibration of the entanglement segments in the direction lateral to the probe backbone.

Furthermore, analysis of the dielectric data of linear PI probe in the DTD-free environment (in long PI matrix) suggests that the dilated tube in monodisperse systems has a dual structure, the partially dilated tube explained above and a thinner, motional path tube wriggling in the partially dilated tube. The motional path tube is deduced by considering the consistent coarse-graining of the time and length scales together with the coherence of the longitudinal motion of the probe chain. The dielectric relaxation time of monodisperse PI in bulk is well described as the time required for the longitudinal chain motion along the path tube, and the viscoelastic relaxation time is described as the time for this motion combined with the lateral equilibration of the entanglement segments (DTD).

The comparison of the viscoelastic and dielectric data allows us to experimentally resolve the detailed features explained above. Nevertheless, some theoretical uncertainties remain, for example, for the molecular origin(s) of the difference in the CR relaxation time of chemically different chains (PI and PS) and for the value of the tube dilation exponent d. These uncertainties are important/interesting subjects of future work.

## IV. ACKNOWLEDGEMENTS

Preparation of this review article was partly supported by the Grant-in-Aid for Scientific Research (B) from JSPS, Japan (grant no. 19H02775). The authors thank Prof. Evelyne van Ruymbeke, Prof. Daniel Read, and Prof. Ronald Larson for their invaluable comments that enabled us to improve this review article.

#### V. REFERENCES

- <sup>1</sup>H. Watanabe, *Prog. Polym. Sci.* **24**, 1253 (1999).
- <sup>2</sup>T. C. B. McLeish, *Adv. Phys.* **51**, 1379 (2002).
- <sup>3</sup>R. Böhmer and F. Kremer, "Dielectric Spectroscopy and Multidimensional NMR—a Comparison," in *Broadband Dielectric Spectroscopy*, F. Kremer and A. Schönhals, Eds., Springer, Berlin, 2003, Ch. 17.
- <sup>4</sup>W. W. Graessley, *Polymeric Liquids and Networks: Dynamics and Rheology*, Garland Science, New York, 2004.
- <sup>5</sup>Q. Huang, O. Mednova, H. K. Rasmussen, N. J. Alvarez, A. L. Skov, K. Almdal, and O. Hassager, *Macromolecules* **46**, 5026 (2013).
- <sup>6</sup>H. Janeschitz-Kriegl, *Polymer Melt Rheology and Flow Birefringence*, Springer, Berlin, 1983.
- <sup>7</sup>W. H. Stockmayer, *Pure Appl. Chem.* **15**, 539 (1967).
- <sup>8</sup>A. Schönhals and F. Kremer, "Theory of Dielectric Relaxation," in *Broadband Dielectric Spectroscopy*, F. Kremer and A. Schönhals, Eds., Springer, Berlin, 2003, Ch. 1.
- <sup>9</sup>A. E. Likhtman, "Viscoelasticity and Molecular Rheology," in *Polymer Science: A Comprehensive Reference*, K. Matyjaszewski and M. Möller, Eds., Elsevier, Amsterdam, Volume 1, pp. 133–179.
- <sup>10</sup>K. Adachi and T. Kotaka, *Prog. Polym. Sci.* **18**, 585 (1993).
- <sup>11</sup>Y. Imanishi, K. Adachi, and T. Kotaka, J. Chem. Phys. 89, 7585 (1988).
- <sup>12</sup>K. Adachi, S. Itoh, I. Nishi, and T. Kotaka, *Macromolecules* 23, 2554 (1990).
- <sup>13</sup>K. Adachi, H. Yoshida, F. Fukui, and T. Kotaka, *Macromolecules* 23, 3138 (1990).
- <sup>14</sup>O. Urakawa, K. Adachi, and T. Kotaka, *Macromolecules* **26**, 2036 (1993).
- <sup>15</sup>O. Urakawa, K. Adachi, and T. Kotaka, *Macromolecules* 26, 2042 (1993).
- <sup>16</sup>O. Urakawa and H. Watanabe, *Macromolecules* **30**, 652 (1997).
- <sup>17</sup>J. S. Fodor, J. R. Huljak, and D. A. Hill, *J. Chem. Phys.* **103**, 5725 (1995).
- <sup>18</sup>D. Boese and F. Kremer, *Macromolecules* 23, 829 (1990).
- <sup>19</sup>D. Boese, F. Kremer, and L. Fetters, *Macromolecules* 23, 1826 (1990).
- <sup>20</sup>C. Riedel, A. Alegria, P. Tordjeman, and J. Colmenero, *Macromolecules* 42, 8492 (2009).
- <sup>21</sup>S. Arrese-Igor, A. Alegría, and J. Colmenero, *Phys. Rev. Lett.* **113**, 078302 (2014).
- <sup>22</sup>T. Glomann, G. J. Schneider, A. R. Bras, W. Pyckhout-Hintzen, A. Wischnewski, R. Zorn, J. Allgaier, and D. Richter, *Macromolecules* 44, 7430 (2011).
- <sup>23</sup>H. Watanabe, *Macromol. Rapid Commun.* **22**, 127 (2001).
- <sup>24</sup>H. Watanabe, *Polymer J.* **41**, 929 (2009).
- <sup>25</sup>H. Watanabe, O. Urakawa, and T. Kotaka, *Macromolecules* **26**, 5073 (1993).
- <sup>26</sup>H. Watanabe, O. Urakawa, and T. Kotaka, *Macromolecules* 27, 3525 (1994).
- <sup>27</sup>H. Watanabe, H. Yamada, and O. Urakawa, *Macromolecules* **28**, 6443 (1995).
- <sup>28</sup>H. Watanabe, M.-L. Yao, and K. Osaki, *Macromolecules* **29**, 97 (1996).
- <sup>29</sup>Y. Matsumiya, H. Watanabe, K. Osaki, and M.-L. Yao, *Macromolecules* 31, 7528 (1998).
- <sup>30</sup>Y. Matsumiya, H. Watanabe, and K. Osaki, *Macromolecules* **33**, 499 (2000).
- <sup>31</sup>H. Watanabe, Y. Matsumiya, and K. Osaki, J. Polym. Sci. Part B: Polym. Phys. 38, 1024 (2000).
- <sup>32</sup>Y. Matsumiya and H. Watanabe, *Macromolecules* 34, 5702 (2001).
- <sup>33</sup>H. Watanabe, Y. Matsumiya, and T. Inoue, *Macromolecules* **35**, 2339 (2002).
- <sup>34</sup>H. Watanabe, S. Ishida, Y. Matsumiya, and T. Inoue, *Macromolecules* 37, 1937 (2004).
- <sup>35</sup>H. Watanabe, S. Ishida, Y. Matsumiya, and T. Inoue, *Macromolecules* 37, 6619 (2004).
- <sup>36</sup>H. Watanabe, T. Sawada, and Y. Matsumiya, *Macromolecules* **39**, 2553 (2006).
- <sup>37</sup>Y. Matsumiya, L. Kumazawa, M. Nagao, O. Urakawa, and H. Watanabe, *Macromolecules* 46, 6067 (2013).
- <sup>38</sup>H. Watanabe, Y. Matsumiya, and E. van Ruymbeke, *Macromolecules* **46**, 9296 (2013).

- <sup>39</sup>Y. Matsumiya and H. Watanabe, Nihon Reoroji Gakkaishi (J. Soc. Rheol. Japan) 42, 235 (2014).
- <sup>40</sup>Y. Matsumiya, Y. Masubuchi, T. Inoue, O. Urakawa, C.-Y. Liu, E. van Ruymbeke, and H. Watanabe, *Macromolecules* **47**, 7637 (2014).
- <sup>41</sup>M. Doi, J. Polym. Sci. Polym. Phys. Ed. 21, 667 (1983).
- <sup>42</sup>W. W. Graessley, Adv. Polym. Sci. 47, 67 (1982).
- <sup>43</sup>G. Marrucci, J. Polym. Sci., Polym. Phys. Ed. 23, 159 (1985).
- <sup>44</sup>Y. Sawada, X. Qiao, and H. Watanabe, Nihon Reoroji Gakkaishi (J. Soc. Rheol. Japan) 35, 11 (2007).
- <sup>45</sup>H. Watanabe and T. Kotaka, *Macromolecules* 17, 2316 (1984).
- <sup>46</sup>H. Watanabe, T. Sakamoto, and T. Kotaka, *Macromolecules* **18**, 1436 (1985).
- <sup>47</sup>H. Watanabe, M. Yamazaki, H. Yoshida, and T. Kotaka, *Macromolecules* **24**, 5573 (1991).
- <sup>48</sup>H. Watanabe, H. Yoshida, and T. Kotaka, *Macromolecules* **25**, 2442 (1992).
- <sup>49</sup>P. F. Green, P. J. Mills, C. J. Palmstrøm, J. W. Mayer, and E. J. Kramer, *Phys. Rev. Lett.* **53**, 2145 (1984).
- <sup>50</sup>P. F. Green and E. J. Kramer, *Macromolecules* **19**, 1108 (1986).
- <sup>51</sup>X. Qiao, T. Sawada, Y. Matsumiya, and H. Watanabe, *Macromolecules* **39**, 7333 (2006).
- <sup>52</sup>H. Watanabe, Q. Chen, Y. Kawasaki, Y. Matsumiya, T. Inoue, and O. Urakawa, *Macromolecules* 44, 1570 (2011).
- <sup>53</sup>J. Klein, *Macromolecules* **19**, 105 (1986).
- <sup>54</sup>D. J. Read, M. E. Shivokhin, and A. E. Likhtman, J. Rheol. **62**, 1017 (2018).
- <sup>55</sup>R. S. Graham, A. E. Likhtman, T. C. B. McLeish, and S. T. Milner, *J. Rheol.* **47**, 1171 (2003).
- <sup>56</sup>H. Watanabe, Y. Matsumiya, E. van Ruymbeke, D. Vlassopoulos, and N. Hadjichristidis, *Macromolecules* **41**, 6110 (2008).
- <sup>57</sup>R. C. Ball and T. C. B. McLeish, *Macromolecules* **22**, 1911 (1989).
- <sup>58</sup>S. T. Milner and T. C. B. McLeish, *Macromolecules* **30**, 2159 (1997).
- <sup>59</sup>S. J. Park and R. G. Larson, *Macromolecules* **37**, 597 (2004).
- <sup>60</sup>E. van Ruymbeke, Y. Masubuchi, and H. Watanabe, *Macromolecules* **45**, 2085 (2012).
- <sup>61</sup>R. Hall, B.-G. Kang, S. Lee, T. Chang, D. C. Venerus, N. Hadjichristidis, J. Mays, and R. G. Larson, *Macromolecules* **52**, 1757 (2019).
- <sup>62</sup>J. L. Viovy, M. Rubinstein, and R. H. Colby, *Macromolecules* **24**, 3587 (1991).
- <sup>63</sup>M. J. Struglinski and W. W. Graessley, *Macromolecules* 18, 2630 (1985).
- <sup>64</sup>E. van Ruymbeke, V. Shchetnikava, Y. Matsumiya, and H. Watanabe, *Macromolecules* 47, 7653 (2014).
- <sup>65</sup>T. Ebrahimi, H. Taghipour, D. Grießl, P. Mehrkhodavandi, S. G. Hatzikiriakos, and E. van Ruymbeke, *Macromolecules* 50, 2535 (2017).
- <sup>66</sup>R. Everaers, S. K. Sukumaran, G. S. Grest, C. Svaneborg, A. Sivasubramanian, and K. Kremer, Science 303, 823 (2004).
- <sup>67</sup>C. Tzoumanekas and D. N. Theodorou, *Macromolecules* **39**, 4592 (2006).
- <sup>68</sup>K. Foteinopoulou, N. Ch. Karayiannis, V. G. Mavrantzas, and M. Kröger, *Macromolecules* **39**, 4207 (2006).
- <sup>69</sup>A. E. Likhtman and M. Ponmurugan, *Macromolecules* **47**, 1470 (2014).
- <sup>70</sup>A. E. Likhtman, *Soft Matter* **10**, 1895 (2014).

[Received August 2019, Revised October 2019]